A&A, 710, A232 (2026)
https://doi.org/10.1051/0004-6361/202659543

Astronomy & Astrophysics

Enhanced activity in close dual-AGN systems in the local Universe

Lorenzo Battistini[1,2,⋆], Alessandra De Rosa[2], Paola Severgnini[3], Cristian Vignali[4,5], Jasbir Singh[3], Pedro R. Capelo[6], Elena Bertola[7], Stefano Bianchi[1], Quirino D'Amato[2], Matteo Guainazzi[8], Fabio La Franca[1], Isabella Lamperti[9,7], Filippo Mannucci[7], Manali Parvatikar[2], Enrico Piconcelli[10], Federica Ricci[1], Fabio Rigamonti[3,11,12], Martina Scialpi[13,9,7], and Maria Vittoria Zanchettin[7]

[1] Dipartimento di Matematica e Fisica, Università degli Studi Roma Tre, Via della Vasca Navale 84, 00146 Roma, Italy
[2] INAF – Istituto di Astrofisica e Planetologia Spaziali (IAPS), Via Fosso del Cavaliere, Roma 1-133, Italy
[3] INAF – Osservatorio Astronomico di Brera, Via Brera 28, Milano 20141, Italy
[4] Dipartimento di Fisica e Astronomia 'Augusto Righi', Università degli Studi di Bologna, Via Gobetti 93/2, I-40129 Bologna, Italy
[5] INAF – Osservatorio di Astrofisica e Scienza dello Spazio di Bologna, Via Gobetti 93/3, I-40129 Bologna, Italy
[6] Department of Astrophysics, University of Zurich, Winterthurerstrasse 190, CH-8057 Zürich, Switzerland
[7] INAF – Osservatorio Astrofisico di Arcetri, Largo E. Fermi 5, I-50125 Firenze, Italy
[8] European Space Agency (ESA), European Space Research and Technology Centre (ESTEC), Keplerlaan 1, 2201 AZ Noordwijk, The Netherlands
[9] Università di Firenze, Dipartimento di Fisica e Astronomia, Via G. Sansone 1, I-50019 Sesto F.no, Firenze, Italy
[10] INAF Osservatorio Astronomico di Roma, Via Frascati 33, 00078 Monte Porzio Catone (RM), Italy
[11] INFN, Sezione di Milano-Bicocca, Piazza della Scienza 3, I-20126 Milano, Italy
[12] Como Lake centre for AstroPhysics (CLAP), DiSAT, Università dell'Insubria, Via Valleggio 11, 22100 Como, Italy
[13] University of Trento, Via Sommarive 14, I-38123 Trento, Italy

Received 20 February 2026 / Accepted 13 April 2026

ABSTRACT

We present a study of an X-ray-selected sample of active galactic nuclei (AGN) in pairs at projected spatial separations $1 < r_p/\mathrm{kpc} < 100$ at $z < 0.1$, using XMM-Newton and Chandra data. We derived the pair sample from an initial pool of approximately 2000 X-ray-selected AGN, and is composed of both AGN-AGN pairs (so-called dual AGN) and AGN-galaxy pairs. From this selection, we find that approximately 10% of AGN reside in pairs, and about 4% are paired with another AGN. We performed a detailed X-ray and SDSS optical spectral analysis for AGN in dual systems and X-ray analysis for AGN in AGN-galaxy pairs, to characterise their absorption properties and investigate the possible triggering mechanisms. We then investigated how obscuration, luminosity, and Eddington ratio depend on projected separation r_p. Amongst all AGN in pair, we find that ~55% are obscured (with hydrogen column density $N_H > 10^{22}\,\mathrm{cm}^{-2}$), amongst which ~6% are Compton-thick ($N_H > 10^{24}\,\mathrm{cm}^{-2}$). The fraction of absorbed AGN is significantly higher in late-stage mergers ($r_p < 30$ kpc) compared to early-stage mergers ($r_p > 60$ kpc). Amongst the AGN pairs, we also observe an average excess relative to a control sample of inactive galaxies in pairs, and this excess significantly increases with decreasing r_p, but only for obscured AGN. Finally, in dual-AGN systems, both the bolometric luminosity and the Eddington ratio of the less massive black hole in the pair increase as the separation decreases. These findings suggest that mergers may play an important role in triggering AGN accretion and activity.

Key words. Galaxy: general – galaxies: active – galaxies: interactions – galaxies: nuclei – galaxies: Seyfert

1. Introduction

The search for and study of dual active galactic nuclei (dual AGN, with projected spatial separation between nuclei $r_p \sim 100\,\mathrm{pc}-100\,\mathrm{kpc}$) is a topic of great interest in modern astrophysics. Dual AGN are key to understanding the co-evolution between galaxies and their central supermassive black holes (SMBHs), with black hole (BH) masses $6 < \log_{10}(M_{BH}/M_\odot) < 9$ (see e.g. Di Matteo et al. 2005; Treister et al. 2012). Dual AGN represent direct precursors of gravitationally bound binary SMBHs at parsec-scale separations (Volonteri et al. 2022). These systems may eventually coalesce and produce gravitational-wave emission that can be detected with pulsar timing arrays (PTAs; e.g. Agazie et al. 2023; EPTA Collaboration et al. 2023) and, at higher frequencies, with the forthcoming Laser Interferometer Space Antenna (LISA; Amaro-Seoane et al. 2023; Colpi et al. 2024) and the Lunar Gravitational Wave Antenna (LGWA; Ajith et al. 2025). One of the most important open questions concerns how AGN are triggered within their host galaxies. Galaxy mergers are thought to drive the fuelling of gas onto the two nuclei, enhancing accretion onto the SMBHs, which become active (Di Matteo et al. 2005; Treister et al. 2012) and increase their average intrinsic luminosity as the separation between the nuclei decreases (Silverman et al. 2011; Kocevski et al. 2012; Koss et al. 2012; Satyapal et al. 2014; Hou et al. 2020; De Rosa et al. 2023). When merging galaxies are very massive, the inflows can even lead to the formation of a direct-collapse SMBH (Begelman et al. 2006; Mayer et al. 2010, 2024). Although dual AGN are a fundamental ingredient in understanding the physics behind the co-evolution between galaxies and their central SMBHs, detecting them remains

⋆ Corresponding author: lorenzo.battistini@inaf.it

highly challenging due to the spatial resolution of current instruments, which does not allow us to resolve closer systems as redshift increases. A further limitation lies in the proper identification of active nuclei, which can often be obscured by a significant amount of cold gas (see De Rosa et al. 2019 for a review of theory and observations of dual AGN). In particular, in a merger-driven AGN triggering scenario, the fuelling of gas that occurs during the merger could strongly obscure the nuclei, especially in the final stages of the merger (Hopkins et al. 2006), thus decreasing the probability of detecting such systems when using ultraviolet (UV) and optical selections. Indeed, samples of dual AGN have been found to suffer from higher obscuration than isolated AGN (De Rosa et al. 2015; Kocevski et al. 2015; Satyapal et al. 2017; Ricci et al. 2017a; De Rosa et al. 2018; Pfeifle et al. 2019; Ricci et al. 2021; Guainazzi et al. 2021; De Rosa et al. 2023). This is also expected from simulations (Blecha et al. 2018), although it is not yet clear how the column density evolves across merger phases. This leads to an incomplete census of dual-AGN systems, highlighting the need for complementary identification techniques across different wavebands (Comerford et al. 2012; Fu et al. 2015; Foord et al. 2021; Mannucci et al. 2022). These include imaging (for spatially resolved systems), spectroscopic diagnostics such as double-peaked [OIII] emission lines (for spatially unresolved systems; Wang et al. 2009; Smith et al. 2010; Ge et al. 2012; Kim et al. 2020), and/or combined methods such as integral field spectroscopy (e.g. Lena 2015; Mannucci et al. 2022; Scialpi et al. 2024), which combine spectroscopy with high-resolution imaging to confirm dual nuclei (see De Rosa et al. 2019, for a detailed description of dual-AGN identification techniques). Given these reasons, it remains difficult to perform statistically significant studies of these sources (especially at lower separations, i.e. $r_{\rm p} < 30$ kpc), which are needed to compare observed dual-AGN properties with simulations. So far, dual-AGN candidates have been identified primarily via optical observations (most of them through optical spectroscopy), but only hundreds of pairs have been confirmed to be real dual AGN through multi-wavelength studies, while the majority (some thousands) are still only candidate dual systems (Pfeifle et al. 2024). X-rays are one of the most efficient ways to detect AGN and hence dual AGN (Padovani 2016), since they allow us to probe the most internal regions of the nucleus, where the primary AGN emission arises. Moreover, although high absorption can affect the 2−10 keV X-ray emission, both intrinsic luminosity and $N_{\rm H}$ can be robustly recovered up to obscuring column densities $N_{\rm H} < 10^{24}\,{\rm cm}^{-2}$.

To investigate the properties of a homogeneous sample of AGN in pairs and the role of galaxy mergers in triggering AGN activity, we present a study of an X-ray-selected sample of AGN in pairs up to redshift $z \sim 0.1$ (with projected spatial separation $r_{\rm p} \sim 1$−100 kpc). Our work is organised as follows: in Section 2, we describe the sample selection; in Section 3, we present the X-ray data reduction and X-ray and optical spectral analysis of the AGN in our samples; we report our results in Section 4; finally, in Section 5, we discuss our findings and summarise our main results. We adopt a concordance cosmology with $H_0 = 70\,{\rm km\,s^{-1}\,Mpc^{-1}}$, $\Omega_\Lambda = 0.7$, and $\Omega_{\rm M} = 0.3$. The errors and upper and lower limits correspond to the 90% confidence level, unless otherwise noted.

2. Sample selection

De Rosa et al. (2023) studied dual AGN in X-rays, analysing a sample of optically selected narrow-line and broad-line AGN candidates in pairs up to $z \sim 0.1$ from Liu et al. (2011), using XMM-Newton (Schartel et al. 2022) and Chandra (Weisskopf 2012) data. The AGN from Liu et al. (2011) were selected using the Sloan Digital Sky Survey (SDSS; York et al. 2000). To confirm the AGN nature, De Rosa et al. (2023) combined multi-wavelength diagnostics using information from optical Baldwin, Phillips & Terlevich (BPT) diagrams (Kauffmann et al. 2003), X-ray 2−10 keV luminosity (González-Martín et al. 2009), and mid-infrared (mid-IR) diagnostics based on the ratio between X-ray and mid-IR fluxes versus hardness ratio (HR; Severgnini et al. 2012). We aimed to enlarge this sample (composed of 34 AGN, 17 pairs) by searching for new AGN pairs using an X-ray-based selection, where the pair can be composed either of two AGN or of one AGN with a non-AGN galaxy companion. We selected our AGN sample by cross-correlating the 4XMM-Newton catalogue (DR14; Webb et al. 2020) and the Chandra Source Catalogue 2 (CSC2; Evans et al. 2010, 2020) with the Millions of Optical Radio/X-Ray Association (MORX, v2) catalogue (Flesch 2024). The latter is an extensive catalogue of 3 115 575 optical sources associated with X-ray and radio sources (including AGN, type-I and II Seyferts, quasars, BL Lac objects, cataclysmic variable stars, galaxies, lensed quasars, and stars) detected with XMM-Newton, Chandra, Swift, ROSAT, VLASS, LoTSS, RACS, FIRST, NVSS, and SUMSS (Truemper 1982; Becker et al. 1995; Mauch et al. 2003; Woniak et al. 2004; Burrows et al. 2005; Shimwell et al. 2017; McConnell et al. 2020; Lacy et al. 2020). An optical reference catalogue such as MORX is necessary to obtain the redshift, which in MORX is provided either as a spectroscopic or a photometric measurement from the literature. For all sources selected in our sample, the redshift is provided by spectroscopic measurements. In this work, to obtain sufficiently high signal-to-noise X-ray data for AGN pairs, we limited our selection to $z < 0.1$ (for a total of 12 391 AGN candidates and 95 032 galaxies, as classified in MORX from the literature).

2.1. AGN selection

For the sources classified as AGN, Seyferts, and quasars in MORX, we cross-matched this catalogue with the XMM-Newton and Chandra source catalogues using a 5″ radius for the match position. We adopted this radius to account for the nominal astrometric uncertainties of both observatories for weak off-axis detections. Thus, by construction, all AGN in our sample are X-ray sources. From now on, we refer to this sample as the sample selected with XMM-Newton+Chandra. For our selection, we imposed thresholds on the X-ray fluxes of $F(2{-}12\,{\rm keV}) > 10^{-15}\,{\rm erg\,s^{-1}\,cm^{-2}}$ and $F(0.5{-}7\,{\rm keV}) > 10^{-16}\,{\rm erg\,s^{-1}\,cm^{-2}}$ for XMM-Newton and Chandra, respectively, given their sensitivity curves (Watson et al. 2001; Evans et al. 2010, 2020). We additionally imposed a 2−10 keV luminosity threshold of $L(2{-}10\,{\rm keV}) > 10^{40}\,{\rm erg\,s^{-1}}$. We chose this threshold to avoid possible contamination from X-ray binaries in the host galaxy, which are typically observed to have 2−10 keV luminosities up to $\sim 10^{38}{-}10^{39}\,{\rm erg\,s^{-1}}$ (Grimm et al. 2002). Moreover, previous studies showed that AGN usually have a higher 2−10 keV luminosity with respect to non-AGN sources (González-Martín et al. 2009). This resulted in 1737 X-ray-selected AGN candidates. In Figure 2, we report all steps performed to select our final samples. For the sources classified as narrow-line AGN in MORX and with an optical spectrum available from the SDSS DR16 (Ahumada et al. 2020, 428 sources), we also verified whether they are classified as AGN in the BPT diagnostic diagram (Kauffmann et al. 2003). Four sources fall within the star-forming region, so we excluded them from the AGN sample. After this step, the effective number of AGN selected through optical and X-ray criteria is 1733. To recover possible 'hidden' AGN amongst the objects classified as galaxy in MORX, we cross-matched the galaxy-classified sample with the XMM-Newton and Chandra catalogues (again, using a 5″ radius for the cross-match and only considering the sources fulfilling our X-ray criteria on flux and luminosity for AGN). This yields 2875 X-ray galaxies that satisfy these requirements. We further applied two additional AGN selection criteria, requiring each source to satisfy at least one of them:

1. X-ray criterion: $L(2{-}10\,\mathrm{keV}) > 10^{42}\,\mathrm{erg\,s^{-1}}$. This is an additional requirement on the luminosity and selects the brightest sources, which are therefore likely AGN (as also previously mentioned; see González-Martín et al. 2009). We stress that these sources are not optically classified as AGN in MORX. Consequently, when relying solely on X-ray luminosity for AGN identification, a more conservative threshold is required.
2. Mid-IR criterion: Mid-IR colours can identify luminous AGN that are hidden in the optical band (Stern et al. 2012; Mateos et al. 2015; Secrest et al. 2015; Andonie et al. 2025). The main difficulty arises when the host-galaxy emission is comparable to AGN emission (as for bright starburst galaxies). Previous studies using Wide-field Infrared Survey Explorer (WISE; Wright et al. 2010) colours revealed that a mid-IR diagnostic based on the WISE $W1-W2$ colour (where $W1$ and $W2$ are the 3.4 µm and 4.6 µm magnitudes, respectively) can be used to identify AGN emission. For example, Stern et al. (2012) identified a threshold based on $W1-W2 > 0.8$, which selects the most luminous AGN, whereas Satyapal et al. (2014b) used $W1-W2 > 0.52$ (which is more inclusive, but more contaminated by strong starburst galaxies). To exclude contamination from strong starburst galaxies in the mid-IR band, Satyapal et al. (2018) performed simulations combining two different WISE colours ($W1-W2$ versus $W2-W3$, where $W3$ is the WISE 11.6 µm magnitude), finding that, unlike starburst galaxies, AGN tend to occupy a precise region in the $W1-W2$ versus $W2-W3$ colour diagram (see Figure 1). We then chose the latter criterion to select AGN amongst the X-ray-detected galaxies.

To summarise, we considered an X-ray-detected galaxy to be an AGN when: (a) it had an observed X-ray luminosity above $10^{42}\,\mathrm{erg\,s^{-1}}$ or (b) it had an observed X-ray luminosity above $10^{40}\,\mathrm{erg\,s^{-1}}$ and satisfied the mid-IR criterion of Satyapal et al. (2018). In this way, we found that 300 galaxies satisfied the above criteria (see Figure 1), and we classified them as AGN (whose number thus increases from 1733 to 2033, see Figure 2). Through this selection, we recovered all AGN from De Rosa et al. (2023), except four. These four AGN were not selected using our criteria for two possible reasons: (1) the source is not included in the MORX catalogue (J094554.4+423818 and J103855.9+392157), or (2) it shows an X-ray luminosity below our imposed threshold (J015235.2−083233 and J163103.4+395015). However, since all four previous sources are classified as AGN in De Rosa et al. (2023) based on their multi-wavelength diagnostics, we included them in our sample. After all these steps, we obtain a total of 2037 X-ray AGN and 94 732 inactive galaxies.

2.2. Pair selection

We selected dual AGN and AGN-galaxy pair samples by computing the angular separation between the nuclei, converting it into a projected spatial separation using the redshift, and

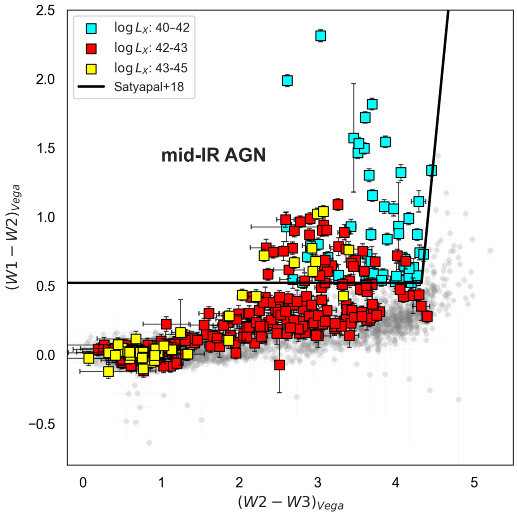

Fig. 1. WISE $W1-W2$ versus $W2-W3$ colour diagram used to select AGN amongst galaxies in MORX. The region identified by the black solid lines is the AGN region according to Satyapal et al. (2018). Squares and faded circles represent the galaxies that passed or did not pass the AGN test described in Section 2.1, respectively. Cyan, red, and yellow squares represent sources with $\log_{10}(L(2{-}10\,\mathrm{keV})/\mathrm{erg\,s^{-1}})$ = 40−42, 42−43, and 43−45, respectively.

imposing a maximum r_p of 100 kpc and a velocity offset $\Delta v < 300\,\mathrm{km\,s^{-1}}$ ($\Delta z < 10^{-3}$). This criterion yields a total of 80 X-ray AGN in pairs (40 pairs), and 46 of them (23 pairs) appeared to be newly identified (Hou et al. 2020; De Rosa et al. 2023). The number of AGN-galaxy pairs is 122. We also identified a control sample of inactive galaxy pairs to compare the statistical properties of AGN and non-AGN pairs. Using the same thresholds for r_p and Δz, we find 2930 inactive galaxies in pairs.

2.3. Final samples

We summarise the selection of AGN-AGN, AGN-galaxy, galaxy-galaxy, and isolated AGN samples as follows (see Figure 2):

- AGN-AGN sample (AA): 80 AGN (40 pairs).
- AGN-galaxy sample (AG): 122 AGN (122 pairs).
- Total AGN pairs sample (TS): 202 AGN (162 pairs). We used this sample when referring to the total number of AGN in pairs (AA+AG).
- Galaxy-galaxy sample (GG): 2930 galaxies (1465 pairs). This is the control sample of non-AGN galaxy-galaxy pairs.
- Parent sample (PS): this is the sample of isolated AGN, obtained as the difference between the total number of X-ray AGN in MORX and the number of AGN found in pairs, for a total of 1835 isolated AGN.

Figure 3 shows the resulting numbers of AGN in the AA, AG, and PS samples. On average, we find that the fraction of AGN with a companion (either another AGN or a galaxy) is ∼10%: the fraction of AGN in AGN-galaxy pairs and in AGN-AGN pairs is ∼6% and ∼4%, respectively (see the table in Figure 3). We defined three different merger stages depending on the separation between the nuclei: late ($r_\mathrm{p} < 30$ kpc), middle (30 kpc $< r_\mathrm{p} <$ 60 kpc), and early ($r_\mathrm{p} >$ 60 kpc) stage of merger[1]. We

[1] This is a simplified distinction, since we do not consider the complete merger history of the two galaxies.

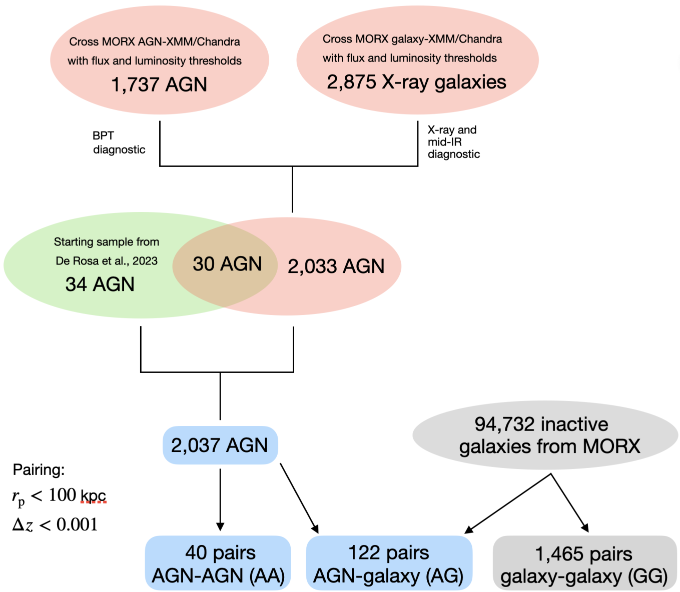

Fig. 2. Sample selection steps and final numbers of AGN and galaxies in pairs.

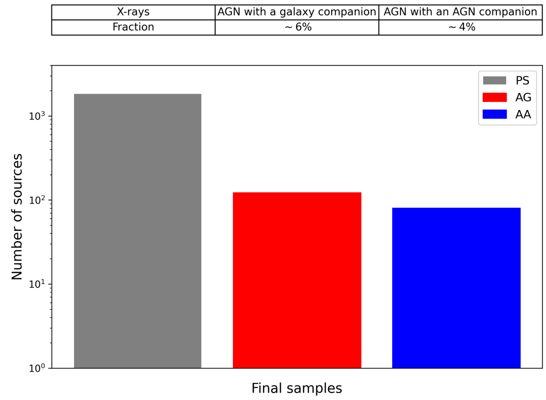

Fig. 3. Sample selection results. The table shows the fractions of AGN in pairs (relative to the total number of AGN), considering all AGN with a galaxy companion and all AGN with an AGN companion. The plot shows the number of isolated AGN (PS), AGN with a galaxy companion (AG), and AGN with an AGN companion (AA) in grey, red, and blue, respectively.

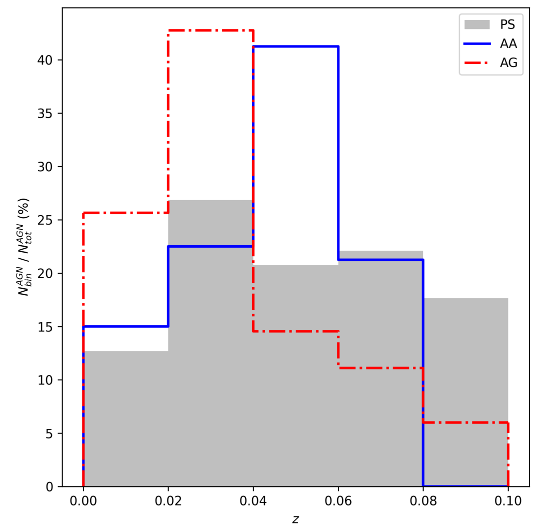

Fig. 4. Redshift distribution of the AGN in the AA (blue histogram), AG (dashed red histogram), and PS (shaded grey histogram). The fraction is computed as the number of AGN in a given redshift bin relative to the total number of AGN in the given sample.

chose the merger stages based on previous observational studies (e.g. Koss et al. 2012; De Rosa et al. 2023) and simulations (e.g. Capelo et al. 2015) on dual AGN, which found that galaxy merger becomes relevant for AGN properties when $r_p \lesssim 30$ kpc. Amongst the pairs in the TS, 94 (~47%) appear to be in a late stage of merger, and most (~70%) are pairs selected with Chandra, as expected from its better angular resolution. The average redshift value for AGN in the AA, AG, and PS samples are ~0.04, ~0.03, and ~0.05, respectively (Figure 4 shows the redshift distributions as blue, red, and grey histograms for the AA, AG, and PS samples, respectively).

3. Data reduction and spectral analysis

Our study includes a combined X-ray and optical spectral analysis of the AA pairs, complemented by an X-ray analysis of the AG pairs. For the AGN in the PS, we also derived the relevant X-ray properties using HR estimates. The results of the X-ray and optical spectral analysis are shown in Table A.1 and A.2, respectively.

3.1. X-ray

For AGN in the AA sample, we extracted XMM-Newton (Chandra) X-ray spectra for AGN in pairs with at least ~50 (~10) counts in the 0.2−12 keV (2−8 keV) EPIC PN (ACIS-S) band. For AGN in the AG sample, given the larger number of sources, we used the spectra available from the XMM-Newton and Chandra archives. We obtain a total of 52 of 80 available X-ray spectra of dual AGN (XMM-Newton+Chandra) and 71 of 122 (XMM-Newton+Chandra) X-ray spectra of AGN in the AG. Amongst dual AGN, 44 (22 pairs) are AGN for which we extracted the spectrum for both nuclei of the pair. For the AGN studied in De Rosa et al. (2023), we used the results derived from their spectral analysis. We used the Science Analysis System (SAS) software V17 (SAS Development Team 2014) for the XMM-Newton data reduction and the Chandra Interactive Analysis of Observations (CIAO) software V4.16 (Fruscione et al. 2006) for the Chandra data reduction. We applied cuts above 10 keV to exclude the flaring particle background for XMM-Newton. We extracted spectra from regions with aperture radii of at least ~20″ and ~1″ for XMM-Newton and Chandra, respectively, to include at least 80% of the source counts at ~1.5 keV for both instruments, given their encircled energy fraction. We extracted source and background regions using the same radius, with the background region selected to avoid contamination from the source. We analysed all spectra using the Xspec V12.14 software (Arnaud 1996) using a χ^2 statistic when spectra had at least 100 (60) net counts in the 0.2−12 keV (0.5−8 keV) band for XMM-Newton (Chandra), and using a Cash statistic (Cash 1979; Wachter et al. 1979) when net counts were lower. When using the χ^2 statistic we required at least 20 (15) counts in each bin for XMM-Newton (Chandra). We assumed the following baseline model (BLM) for the X-ray emission of our AGN:

– a primary X-ray emission of the AGN corona in the 2−10 keV band due to the comptonisation of photons from

the accretion disc of the SMBH (Haardt & Maraschi 1993; Haardt et al. 1994; Ursini et al. 2023; Gianolli et al. 2023). This component can be described by a power law;
- an absorption component from neutral gas with a column density $N_{\rm H}$, which obscures the primary AGN emission;
- a soft X-ray emission, below ∼2 keV, approximated with a power law in most spectra. For obscured AGN, this component could be attributed to emission from the narrow-line region (see, e.g. Bianchi et al. 2019), scattering of the primary emission of the AGN (Ueda et al. 2007), or star formation in the host galaxy (Ranalli et al. 2002); for unobscured AGN, this component could be attributed to reflection processes from the inner parts of the accretion disc and/or absorption from an outflowing warm gas (Miniutti & Fabian 2004; Gierliński & Done 2004; Chen et al. 2025);
- an absorption due to the Milky Way column density along the line of sight (HI4PI Collaboration 2016).

Therefore, our BLM in Xspec is *TBabs*×(*zTBabs*×*powerlaw*^{H} + *powerlaw*^{S}), which has the form

$$f(E) = e^{-N_{\rm H}^{\rm Gal}\sigma}\left(e^{-N_{\rm H}\sigma}K^H E^{-\Gamma^H} + K^S E^{-\Gamma^S}\right),$$

where $N_{\rm H}^{\rm Gal}$ is the hydrogen column density of the Milky Way, σ is the photoelectric absorption cross-section (Balucinska-Church & McCammon 1992), $N_{\rm H}$ is the hydrogen column density obscuring the AGN, K is the normalisation of the power law at 1 keV, and Γ is the photon index of the power law. The superscripts H and S refer to the hard (primary, 2−10 keV) and soft (<2 keV) components, respectively. For 18 spectra, we only required one power law to model the data. In ten sources, the spectrum showed evidence of reflection features believed to be produced by reprocessing of the primary AGN emission from the molecular torus (Antonucci 1993; Jaffe et al. 2004; Meisenheimer et al. 2007; Raban et al. 2009), the broad-line and narrow-line regions (Bianchi et al. 2008; Ponti et al. 2013), or the accretion disc (George & Fabian 1991; Matt et al. 1991). Such features usually appear as emission line components, such as the Fe Kα line at 6.4 keV and a Compton hump above ∼10 keV, peaking at ∼30 keV. In such cases, we added the Fe Kα line as a Gaussian profile and used the *pexrav* model in Xspec to reproduce only the reflection component above ∼10 keV. The *pexrav* model is an exponentially cut-off power-law spectrum reflected from a neutral material (Magdziarz & Zdziarski 1995). When a simple power-law model was not sufficient to reproduce the soft X-ray emission, we used the *Mekal* model as an additive component. This model is an emission spectrum of hot diffuse gas that includes several emission lines (Mewe et al. 1985, 1986; Liedahl et al. 1995). When performing the fits, we typically allowed Γ^H and $N_{\rm H}$ to vary, while the value of Γ^S was usually fixed to that of Γ^H. When it was not possible to simultaneously estimate Γ^H and $N_{\rm H}$, or their associated errors, we fixed the photon-index value to a typical value of 1.9, as observed in large populations of local AGN (Nandra & Pounds 1994; Bianchi et al. 2009; Akylas & Georgantopoulos 2021).

3.2. Optical

For the optical analysis, we considered dual AGN in the AA sample for which both nuclei have an optical spectrum from SDSS DR16: 46 AGN in 23 of the 40 pairs in the GS. This choice was motivated by the goal of comparing the properties of the two BHs in each pair, as described in Section 4. We analysed the optical spectra using the penalised pixel-fitting (pPXF) method by Cappellari (2017), which allows fitting of stellar kinematics and gas optical emission lines. For the stellar population, we used the E-MILES templates (Vazdekis et al. 2016). When performing the fits, we chose the noise level to obtain χ^2/d.o.f. ∼ 1 for each spectrum, assuming constant noise per pixel. For the fitting procedures, we treated the stellar models and gas emission lines as separate components. The emission-line components include the narrow Balmer and [OIII]5007 Å lines, which we used to estimate the bolometric luminosities of sources without X-ray spectral analysis, as described below. Since all sources except one (J103853.29+392151.1[2]) show only narrow emission lines, we used the stellar velocity dispersion (σ^*) obtained from fitting the stellar kinematic component to estimate the BH mass. To do this, we used the relation from McConnell & Ma (2013):

$$\log_{10}\left(\frac{M_{\rm BH}}{{\rm M}_\odot}\right) = (8.32 \pm 0.05) + (5.64 \pm 0.32)\log_{10}\left(\frac{\sigma^*}{200\,{\rm km\,s^{-1}}}\right). \tag{1}$$

Using these mass estimates, we derived the corresponding Eddington (1916) luminosity ($L_{\rm Edd}$) of each AGN in the 23 pairs with an optical spectrum. We then estimated their bolometric luminosity ($L_{\rm bol}$), which is required to compute the Eddington ratio ($\lambda_{\rm Edd}$, defined as $L_{\rm bol}/L_{\rm Edd}$). We adopted the bolometric correction factor from Duras et al. (2020), which uses AGN X-ray luminosity, for the AGN which also had X-ray spectral analysis. When the AGN counts were too low to allow X-ray spectral extraction and analysis (see Section 3.1), we used the bolometric luminosity estimate from Netzer (2009), which requires the narrow Hβ and [OIII]5007 Å fluxes and the extinction-corrected Hβ luminosity (described below). The observed fluxes and luminosities cited above were measured by fitting the gas emission lines with pPXF. Additionally, to correct the Hβ luminosity, we estimated the dust reddening correction $E(B-V)$ using the extinction law of Cardelli et al. (1989), assuming a dust screen and Case-B recombination at a gas temperature of 10^4 K (Osterbrock & Ferland 2006). For one AGN without X-ray spectral analysis (J011832.8–000936), the SDSS spectrum shows a gap between ∼6200 Å and ∼7000 Å, where the Hα line lies. Thus, for this source, we corrected the Hβ luminosity considering the mean $E(B-V)$ ∼ 0.3 value in our sample. For sources with both X-ray and optical information, the derived bolometric luminosities are consistent.

4. Results

In this section, we present the main results of our selection and analysis. In particular, we focus on the absorption properties of dual AGN in the AA and AG samples (Section 4.1) and their triggering mechanisms (e.g. luminosity and accretion properties; Section 4.2). We computed all uncertainties on fractions using binomial errors. When we computed the fractions using values from spectral analysis (e.g. $N_{\rm H}$), we propagated the uncertainties by considering the binomial error and the error derived from the spectral analysis.

[2] Our mass measurement for this source is consistent, within the uncertainties, with that obtained in De Rosa et al. (2018) using single-epoch mass estimates.

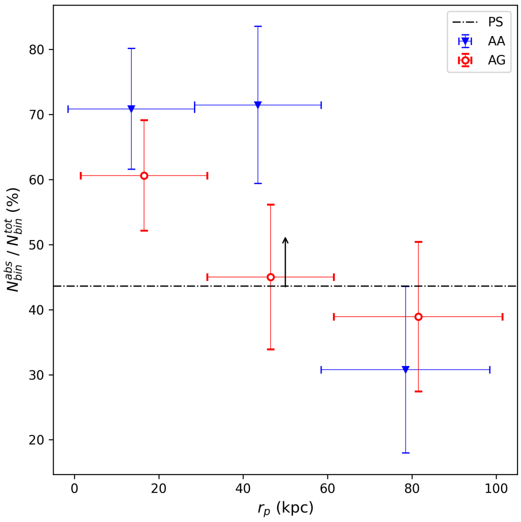

Fig. 5. Fraction of absorbed ($N_H \geq 10^{22}\,cm^{-2}$) AGN in the AA sample (blue data) and AG sample (red data) in bins of 0−30 kpc (late stage of merger), 30−60 kpc (middle stage of merger), and 60−100 kpc (early stage of merger). Fractions are computed as $N^{abs}_{bin}/N^{tot}_{bin}$, where N^{abs}_{bin} and N^{tot}_{bin} are the numbers of AGN with $N_H \geq 10^{22}\,cm^{-2}$ in the given bin and the total number of AGN in that bin, respectively. For AGN in the AA and AG samples, the fractions are computed using N_H from spectral analysis, while for AGN in the PS (dashed, horizontal line) the fraction is estimated as a lower limit through XMM-Newton HR3 and HR4.

4.1. Absorption properties

4.1.1. Absorption properties from spectral analysis

One of the main goals of our work was to study the absorption properties of AGN in pairs in the AA and AG samples, and to compare them with those of isolated AGN in the PS. Using spectral analysis, we measured the column density of 52 and 71 AGN in the AA and AG, respectively. We find fractions of absorbed AGN ($N_H \geq 10^{22}\,cm^{-2}$) of 61 ± 7% in the AA sample and 51 ± 8% in the AG sample, while the fraction of Compton-thick (CT; $N_H > 10^{24}\,cm^{-2}$) AGN is 8 ± 4% (4 ± 2%). Our classification of obscured and unobscured AGN is robust against the presence of N_H upper and lower limits derived from spectral analysis. Specifically, all lower limits are associated with obscured sources, while all upper limits correspond to unobscured sources, ensuring that the relative fractions remain unchanged. The fractions found for dual AGN agree well with previous studies on dual AGN (Koss et al. 2011; Ricci et al. 2017a, 2021; De Rosa et al. 2023) and are generally higher than the fractions of Compton-thin AGN found in samples of isolated AGN using other surveys (e.g. ∼45% using BAT, Krimm et al. 2013; Ricci et al. 2015). The fraction of CT AGN in pairs found in our study (and similarly the ∼16% reported by De Rosa et al. 2023) is lower than that reported in some studies of isolated AGN. For example, Boorman et al. (2025) studied a homogeneous sample of isolated AGN ($z < 0.044$) using the NuSTAR (Harrison et al. 2013) local AGN N_H distribution survey (NULANDS), finding a fraction of ∼35% of CT AGN. It is worth noting that estimating such obscuration regimes is highly challenging when using instruments such as XMM-Newton and Chandra. In fact, when $N_H \gtrsim 10^{24}\,cm^{-2}$, the primary component of the AGN is suppressed up to 10 keV, which is the energy limit accessible with XMM-Newton and Chandra at $z < 0.1$. Thus, the fraction of CT AGN in pairs we found in this analysis should be regarded as a lower limit. To investigate a possible evolution of the obscuration with merger stages in AGN pairs, we estimated the fractions of obscured AGN (considering only those with a measured N_H) in bins of projected spatial separations r_p (see Figure 5). We computed the fractions as $N^{abs}_{bin}/N^{tot}_{bin}$, where N^{abs}_{bin} and N^{tot}_{bin} are the number of absorbed AGN and the total number of AGN in the given bin, respectively. We chose bins of <30 kpc (late stage of merger), 30−60 kpc (middle stage of merger) and 60−100 kpc (early stage of merger). For AGN in the AA sample (blue data points in Figure 5), we find that the fraction of absorbed AGN is higher at the smallest separations (0−30 kpc and 30−60 kpc), where it reaches ∼70% for AA AGN in the late stage of merger. Conversely, in the early stage of merger, the fraction of absorbed AGN is significantly lower, at ∼30%. Moreover, the fraction of obscured AGN in the late stage of merger is significantly higher than the fraction of obscured isolated AGN in the PS estimated through the HR (although we stress that the latter fraction remains a lower limit; see Section 4.1.2). For the AG sample, the error bars prevent us from identifying a clear trend in the obscured fraction with separation (red data points in Figure 5). However, there is marginal evidence for an increase in the obscured AGN fraction across the merger stages, although it is slightly lower than that observed for the dual-AGN sample. A similar result for AGN paired with galaxies has also been identified in previous studies using X-ray data (e.g. Guainazzi et al. 2021, where N_H increases as r_p decreases). These findings suggest that mergers affect AGN obscuration, likely through increased gas fuelling within the two galaxies, as expected from simulations (Hopkins et al. 2006; Capelo & Dotti 2017; Blecha et al. 2018; Volonteri et al. 2022; for a recent review, see Capelo et al. 2023) and as found in previous studies on dual AGN (De Rosa et al. 2015; Kocevski et al. 2015; Ricci et al. 2017b; Satyapal et al. 2017; De Rosa et al. 2018; Pfeifle et al. 2019; Guainazzi et al. 2021; Ricci et al. 2021).

4.1.2. Absorption properties from the HR

To estimate the fraction of Compton-thin AGN in the PS and to compare it with the fractions derived from the spectral analysis of the AA and AG samples, we carried out XMM-Newton simulations in Xspec. These simulations quantify the correlation between HR3 (energy bands 1−2 keV and 2−4.5 keV) and HR4 (energy bands 2−4.5 keV and 4.5−10 keV) and the column density N_H. We describe the simulations in detail in Appendix B. We used HR3 values to distinguish between unobscured and obscured AGN, while we used HR4 to identify highly obscured AGN ($N_H = 10^{23}$–$10^{24}\,cm^{-2}$) that could be missed using only 'soft' HR3. From the simulations (described in Appendix B; see Figure B.1), we consider sources having HR3 > 0 and HR4 > 0.2 as absorbed with $N_H > 10^{22}\,cm^{-2}$ and highly absorbed with $10^{23} \leq N_H/cm^{-2} \leq 10^{24}$, respectively. In the PS, 949 AGN are detected with XMM-Newton and have HR3 and HR4 available from the catalogue. Using the HR3 and HR4 thresholds above, we find that ≳44% of AGN in the PS sample are absorbed. This fraction (although a lower limit) is consistent, within the error bars, with the fraction of obscured AGN in the early stage of merger found in the AA and AG samples through spectral analysis. Moreover, this result is also consistent with the fraction (∼45%) of Compton-thin isolated AGN found in BAT (Krimm et al. 2013; Ricci et al. 2015), as previously mentioned. We stress that even combining HR3 and HR4 values does not allow reliable identification of CT AGN. Thus, these fractions should be considered as lower limits. However, the same bias in identifying CT AGN also arises in the spectral analysis when using XMM-Newton and Chandra, as already discussed. This yields broadly comparable results between spectral analysis and HR-based estimates.

4.2. AGN triggering

4.2.1. Fraction of AGN in pairs

To investigate the triggering mechanisms of AGN in pairs, we first examine the AGN fractions derived from our sample selection. As mentioned in Section 2, we find a fraction ($N^{\rm AGN}_{\rm pair}/N^{\rm AGN}_{\rm tot}$) of AGN in pairs (including both dual AGN and AGN-galaxy pairs) of ~10% of all X-ray-selected AGN below 100 kpc (4% for late-stage mergers, i.e. for separations below 30 kpc). Within this fraction, ~4% (~2% for late-stage mergers) are dual AGN (see Figure 3). These fractions are in agreement with previous studies of dual AGN in the X-ray band at low redshift (e.g. He et al. 2023). To investigate the connection between AGN activity and galaxy mergers, we quantified the excess of AGN pairs in the TS relative to the incidence of galaxy pairs in the GG sample. We computed the excess in bins of projected separation with a width of 20 kpc. For each bin in $r_{\rm p}$, we defined the excess as $f_{\rm AGN}/f_{\rm gal}$, where $f_{\rm AGN}$ and $f_{\rm gal}$ represent the fractions of AGN and galaxies in pair in that separation bin, respectively. We calculated these fractions as

$$f_{\rm AGN} = \frac{N^{\rm AGN,TS}_{\rm bin}}{N^{\rm AGN}_{\rm tot}}, \qquad f_{\rm gal} = \frac{N^{\rm gal,GG}_{\rm bin}}{N^{\rm gal}_{\rm tot}},$$

with $N^{\rm AGN,TS}_{\rm bin}$ and $N^{\rm gal,GG}_{\rm bin}$ being the number of AGN and galaxies in pairs within the corresponding $r_{\rm p}$ bin. We evaluated the excess considering, for both $N^{\rm AGN,TS}_{\rm bin}$ and $N^{\rm AGN}_{\rm tot}$: the total number of AGN, the number of obscured AGN, and the number of unobscured AGN. For the latter two, we considered the obscuration found through X-ray spectral analysis for AGN pairs, and HR-based estimations for isolated AGN, see Section 4.1. The total number for galaxies is $N^{\rm gal}_{\rm tot} = 94\,732$, so that $f_{\rm gal}$ is constant (in the corresponding bin) for all three groups of AGN (total, obscured, and unobscured). Instead, $N^{\rm AGN}_{\rm tot}$ depends on the AGN classification used to evaluate the excess and corresponds to 2037 for all AGN, 874 for obscured AGN, and 1083 for unobscured AGN. All total numbers include both paired and isolated AGN (or galaxies). Figure 6 shows the AGN-pair excesses. We find an average excess of ~3 for all AGN (obscured and unobscured) with respect to galaxies in pairs. That suggests that AGN are, on average, more common than inactive galaxies when in pairs. However, the excess for the total AGN sample in TS does not show a significant trend with separation (Spearman $\rho \sim -0.4$, p-value ~0.5; see the purple line in Figure 6). If we separate the excess for obscured and unobscured AGN (red and blue lines in Figure 6, respectively), a significant increase in the excess with decreasing $r_{\rm p}$ is found for obscured AGN (with Spearman $\rho \sim -0.9$, p-value ~0.04). The same trend is not observed for unobscured AGN. This suggests that obscured AGN are more common in pairs with respect to galaxies, especially at the smallest separations, as expected from simulations (Capelo et al. 2017). These results are consistent with the higher fraction of obscured AGN at the smallest separations found from X-ray spectral analysis (see Figure 5), and suggest that galaxy mergers may play an important role in triggering AGN activity and enhancing nuclear obscuration. Similar results have been reported in other studies on AGN in pairs (Gao et al. 2020; Ellison et al. 2025), which find an increase in narrow-line and mid-IR-selected AGN excess with decreasing $r_{\rm p}$ that peaks shortly after the coalescence phase).

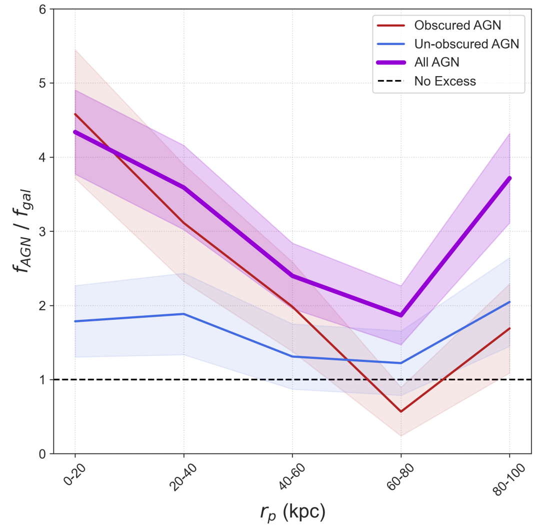

Fig. 6. Excess of AGN pairs in TS with respect to galaxy pairs (GG) as a function of the projected spatial separation. The excess is defined as $f_{\rm AGN}/f_{\rm gal}$, where $f_{\rm AGN}$ is the fraction of AGN in pairs in a given bin relative to the total number of AGN (pairs plus isolated), and $f_{\rm gal}$ is defined analogously for galaxy pairs. The purple line represents the excess for all AGN in TS, whereas the red and blue lines show the AGN excess for obscured and unobscured AGN, respectively, based on the results from the X-ray spectral analysis. The horizontal black dashed line represents the no-excess case.

4.2.2. AGN luminosity and accretion

Obscured AGN in pairs tend to lie at the smallest separations (see Section 4.2.1 and Figure 5). This suggests that, at close separations, galaxy nuclei may experience enhanced gas inflows, increasing the amount of material available to fuel SMBH accretion. In this scenario, AGN activity may be more efficiently triggered when the nuclei are closer together, leading to higher intrinsic luminosities. To investigate this behaviour, we tested whether dependencies exist between the AGN bolometric luminosity ($L_{\rm bol}$), BH mass ($M_{\rm BH}$), and Eddington ratio ($\lambda_{\rm Edd}$) as a function of $r_{\rm p}$. For each quantity X (with $X = L_{\rm bol,1}$, $L_{\rm bol,2}$, $M_{\rm BH,1}$, $M_{\rm BH,2}$, $\lambda_{\rm Edd,1}$, or $\lambda_{\rm Edd,2}$, where 1 and 2 refer to the more massive (primary) and less massive (secondary) BH of each pair, respectively), when a correlation with projected separation was identified using a Spearman test, we searched for a linear correlation using the following:

$$\log_{10}(X) = \alpha \cdot \left(\frac{r_{\rm p}}{100\,{\rm kpc}}\right) + \beta, \tag{2}$$

where α and β (and their associated errors) were estimated from the fit. Table 1 summarises the best-fit parameters. In our sample, the source J085125.8+393541 is an intermediate-mass BH (IMBH) in an early stage of merger (diamond data point in the left-hand panels of Figures 7 and 8), with a BH mass $\log_{10}(M_{\rm BH}/{\rm M}_\odot) = 4.6 \pm 0.6$. This source has been studied in previous works and was found to be hosted in a dwarf galaxy of stellar mass $\log_{10}(M_*/{\rm M}_\odot) = 9.41$ and to host a BH mass with mass $\log_{10}(M_{\rm BH}/{\rm M}_\odot) = 5.4$ (Reines et al. 2013), estimated using the full width at half maximum (FWHM) of the Hα line and its luminosity following the approach of Greene & Ho

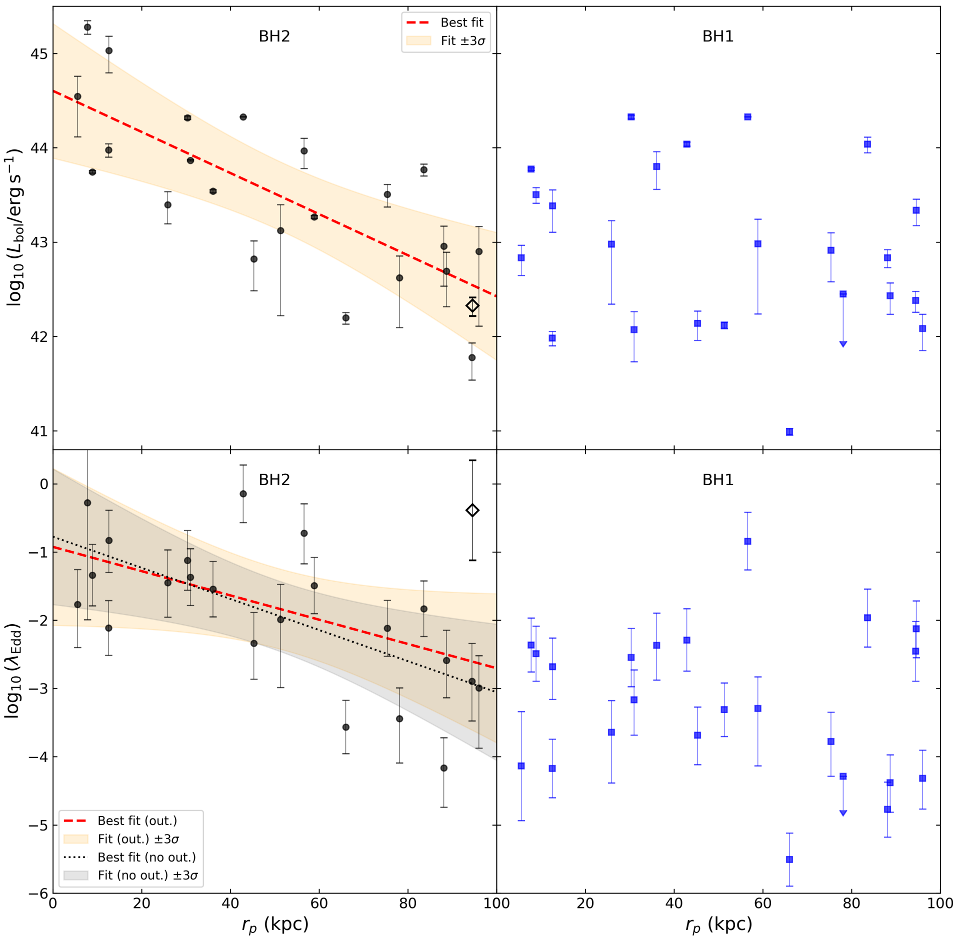

Fig. 7. Bolometric luminosity and Eddington ratio as a function of projected spatial separation. Top left: Bolometric luminosity of BH2 as a function of projected spatial separation. The dashed red line and shaded yellow band represent the best-fit relation and its uncertainty region at $\pm 3\sigma$. Top right: Bolometric luminosity of BH1 as a function of projected spatial separation. Bottom left: Eddington ratio of BH2 as a function of the projected spatial separation. The dashed red (dotted black) line and the shaded yellow (grey) area represent the best-fit relation and its uncertainty region at $\pm 3\sigma$, including (excluding) the IMBH J085125.8+393541. Bottom right: Eddington ratio of BH1 as a function of the projected spatial separation.

(2005) and Bentz et al. (2013). Moreover, this source was also classified as an AGN using a luminosity-based X-ray method Wasleske & Baldassare (2024). Given the peculiar nature of this AGN, we treated it as an outlier in our correlation tests.

When considering the more massive BH (BH1) and the less massive one (BH2) separately, we find a clear anti-correlation between the bolometric luminosity of BH2 and r_p (see the top left-hand panel of Figure 7), with a Spearman coefficient $\rho \sim -0.77$ and a p-value of $\sim 2 \times 10^{-5}$. Conversely, the bolometric luminosity of BH1 ($L_{bol,1}$) remains approximately flat during the merger phases (see the top right-hand panel of Figure 7), with $\rho \sim -0.23$ and a p-value of ~ 0.29, indicating no correlation[3]. Given the significance of the correlation for $L_{bol,2}$ with r_p, we then searched for a linear relation using Equation (2). The linear fit between $\log_{10}(L_{bol,2})$ and r_p yields

$$\log_{10}\left(\frac{L_{bol,2}}{\mathrm{erg\,s^{-1}}}\right) = (-2.2 \pm 0.4) \cdot \left(\frac{r_p}{100\,\mathrm{kpc}}\right) + (44.60 \pm 0.24), \quad (3)$$

with a standard deviation of $\sigma_{res} = 0.56$ dex. This shows that in the late merger stages, AGN could reach luminosities more than three orders of magnitude higher than those in early stages. Moreover, there is no evidence for increasing BH mass with decreasing r_p for either BH1 and BH2 (Spearman coefficients $\rho \sim -0.01$ and $\rho \sim -0.11$, respectively), as shown in the left-hand panel of Figure 8. This suggests that the increase in bolometric luminosity of BH2 is not driven by a systematically higher-mass BH population at the smallest separations, but instead may reflect enhanced accretion triggered by nuclear interaction, in agreement with De Rosa et al. (2023). This result shows that galaxy mergers in our sample play a role in triggering AGN activity in the most luminous AGN. The top left-hand panel of Figure 7 shows the best-fit for $L_{bol,2}$ and its uncertainty region at $\pm 3\sigma$ as a dashed red line and a shaded yellow band, respectively.

To exclude possible biases in relation (3) due to selection effects at the smallest separations, we performed simulations to quantify the number of potentially missing low-luminosity AGN in our sample. This is particularly relevant for the late-stage merger regime, where a higher fraction of obscured AGN

[3] For $L_{bol,2}$ we omit the results obtained when excluding the outlier, as the correlation significance shows no appreciable changes.

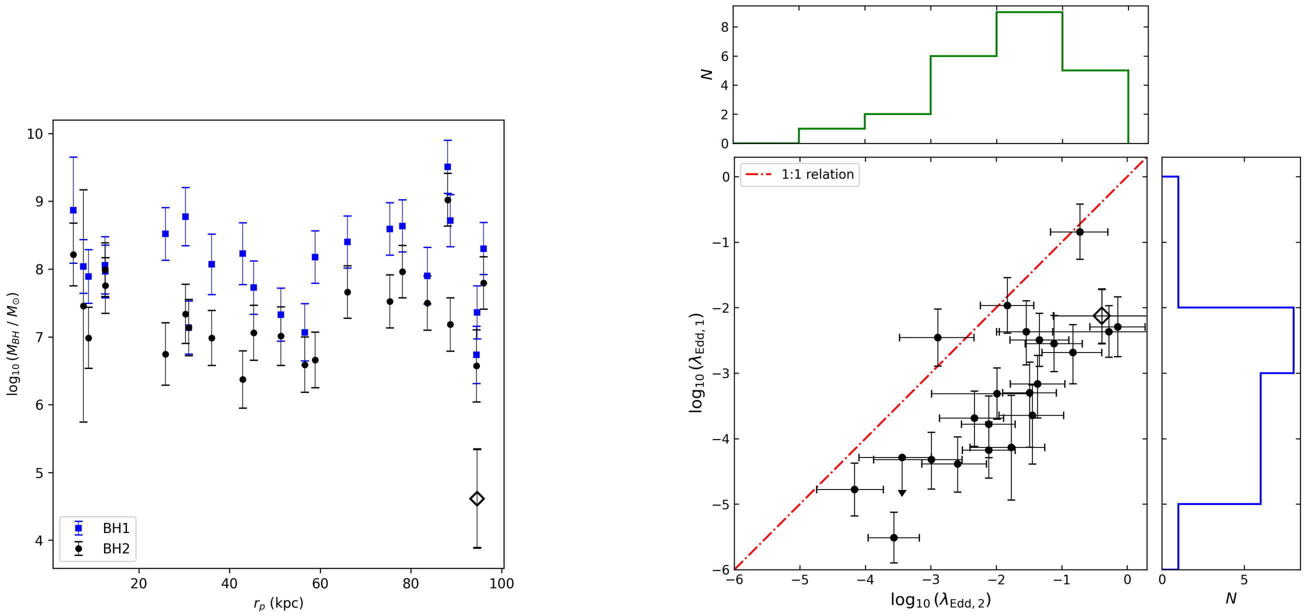

Fig. 8. Left-hand panel: mass of BH1 (blue squared data-points) and BH2 (black circled data-points) for AGN in the AA as a function of the projected spatial separation. Right-hand panel: Eddington ratio of the more massive BH of the pair versus the Eddington ratio of the less massive BH, computed through the spectral analysis. The red dashed line is the 1:1 relation. The blue and green histograms show the distribution (in terms of number of sources N) of $\log_{10}(\lambda_{\rm Edd,1})$ and $\log_{10}(\lambda_{\rm Edd,2})$, respectively. For both panels, the diamond data point is the IMBH J085125.8+393541.

is expected, as described in Sections 4.1 and 4.2.1. This could lead to a lack of low-luminosity AGN that are not detected with XMM-Newton and Chandra, because their X-ray fluxes are below the sensitivity limit of the available observations (see Section 2.1). Our simulations (described in detail in Appendix C) revealed that the potential lack of low-luminosity AGN (relative to all detected AGN in the same bin of r_p) corresponds to less than ~8% in the late and middle merger stages and less than ~5% in the early stage. This is visible in Figure C.1, where the increase in bolometric luminosity in the first r_p bin after imposing flux cuts to match our observed sample is marginal and not significant (less than 0.1 dex). This further test suggests that the anti-correlation between $\log_{10}(L_{\rm bol,2})$ and r_p is due to physical mechanisms occurring during the merger and not to a selection effect.

To investigate the way through which two galaxies in a pair co-evolve, we examined the Eddington ratios of our dual AGN, a parameter which is crucial to study the accretion properties of the SMBH (Salpeter 1964; Lynden-Bell 1969; Shakura & Sunyaev 1973; Soltan 1982; Rees 1984) and its growth (Heckman et al. 2004; Aird et al. 2012). First, we compared the Eddington ratios between the more massive SMBH ($\lambda_{\rm Edd,1}$) and the less massive SMBH ($\lambda_{\rm Edd,2}$) within each pair. As was also found in previous studies (e.g. Bernhard et al. 2018; Aggarwal 2024), the less massive BH of each pair shows, in the vast majority of cases, the highest $\lambda_{\rm Edd}$, which is indicative of a higher accretion occurring in the less massive SMBH (see Figure 8). In fact, what arises when comparing sources 1 and 2 is the different peak of the respective Eddington ratio distributions (see the blue and green histograms in Figure 8). The mean values for $\langle\log_{10}(\lambda_{\rm Edd,1})\rangle$ and $\langle\log_{10}(\lambda_{\rm Edd,2})\rangle$ are ~-3.1 and ~-1.8, with standard deviation $\sigma_{\rm std} = 1.07$ and $\sigma_{\rm std} = 1.05$, respectively.

To investigate whether mergers impact accretion onto SMBHs in pairs, we searched for a dependence of the Eddington ratios on the projected spatial separation between the two nuclei of each pair. As a result, in Figure 7, the Eddington ratios of sources two and one (bottom left-hand and bottom right-hand panels, respectively) are shown as a function of the projected spatial separation of the pair. Figure 7 shows an increase in $\lambda_{\rm Edd,2}$ as the separation between the two nuclei decreases. In contrast, the Eddington ratios of source one do not show this trend occurring during the merger phases. This agrees with the increase in bolometric luminosity of source two with decreasing r_p, and with the flat $\log_{10}(L_{\rm bol,1})$–r_p relation shown in the top panels of Figure 7. Considering that most mergers in our dual-AGN sample are minor mergers (i.e. $M_{\rm BH,2}/M_{\rm BH,1} \leq 0.25$), this result agrees with the hydrodynamical simulations by Capelo et al. (2015). In those simulations, a clear dependence of bolometric luminosity and Eddington ratio on separation is observed, especially for minor mergers, albeit at different length scales, with the decrease confined to $\lesssim$10-kpc scales. Not accounting for several other possible differences between observed and simulated galaxies (e.g. morphology, environment, and orbital parameters), we note that the mass of the simulated BHs was in the range 0.4–4×10^6 M$_\odot$, whereas the observed BHs mostly lie in the range $\sim 10^7$–10^9 M$_\odot$ (see the left-hand panel of Figure 8), approximately two orders of magnitude more massive. Assuming that the galactic mass also increases by a similar factor (e.g. Reines & Volonteri 2015) and adopting a simple mass-radius quadratic relation (e.g. Schulz 2017), we infer galactic sizes larger by a factor of ~10. Assuming that a galaxy is significantly perturbed only when the separation R between the two galaxies (of masses m and M, with $m < M$) is on the order of the tidal radius ($r_{\rm tidal} \simeq R(m/3M)^{1/3}$, for $m \ll M$), and adopting the same galaxy mass ratio as in Capelo et al. (2015), we surmise that simulations of these larger systems would show interactions between the two galaxies starting (and progressing; including the hydrodynamical torque effects caused by the expanded ram-pressure shock region, see Capelo & Dotti 2017) at larger distances, by a factor of ~10. This would stretch the simulated luminosity-distance relation by the same factor and thus resemble the observed relation.

Table 1. Best-fit results correlating $L_{\rm bol}$, $M_{\rm BH}$, and $\lambda_{\rm Edd}$ with $r_{\rm p}$ for BH2 and BH1 (using Equation 2). For $\lambda_{\rm Edd,2}$, results include and exclude the outlier (out.) IMBH J085125.8+393541.

X	$^{(a)}\alpha$	$^{(b)}\beta$	$^{(c)}\sigma_{\rm res}$ (dex)	$^{(d)}\rho$	$^{(e)}p$-value	$^{(f)}$Mean
$L_{\rm bol,2}$	-2.2 ± 0.4	44.60 ± 0.24	0.560	−0.77	2×10^{-5}	2×10^{44} erg s^{-1}
$^*L_{\rm bol,1}$	–	–	–	−0.22	0.11	4×10^{43} erg s^{-1}
$^*M_{\rm BH,2}$	–	–	–	−0.15	0.49	7.8×10^{7} M$_\odot$
$^*M_{\rm BH,1}$	–	–	–	−0.02	0.94	3.4×10^{8} M$_\odot$
$\lambda_{\rm Edd,2}$ (out.)	-1.8 ± 0.6	-0.92 ± 0.38	0.897	−0.52	0.01	−1.8
$\lambda_{\rm Edd,2}$ (no out.)	-2.3 ± 0.6	-0.78 ± 0.33	0.765	−0.67	7×10^{-4}	−1.9
$^*\lambda_{\rm Edd,1}$	–	–	–	−0.16	0.46	−3.1

Notes. (a, b) Slope and intercept of the best-fit relation; (c) Standard deviation; (d) Spearman or Pearson coefficient. For parameters for which a linear best-fit was found, ρ corresponds to the Pearson coefficient, while for parameters with no correlation with $r_{\rm p}$ it corresponds to the Spearman coefficient (these parameters are marked with *); (e) p-value; (f) Mean value of the quantity.

The Spearman test between $\lambda_{\rm Edd,1}$, $\lambda_{\rm Edd,2}$, and $r_{\rm p}$ indicates a moderate anti-correlation between $\lambda_{\rm Edd,2}$ and $r_{\rm p}$ (both including and excluding the outlier), which is not found for $\lambda_{\rm Edd,1}$ and $r_{\rm p}$ (see Table 1). By fitting the $\lambda_{\rm Edd,2}$–$r_{\rm p}$ relation using Equation (2), we find a linear anti-correlation when including the outlier IMBH J085125.8+393541, with a Pearson coefficient of $\rho \sim -0.52$ and a standard deviation $\sigma_{\rm res} = 0.897$ dex, with a p-value of ~0.01. If the outlier is excluded, we obtain $\rho \sim -0.67$, $\sigma_{\rm res} \sim 0.765$, and a p-value of $\sim 7 \times 10^{-4}$ (see Table 1). In the following, we show only the best-fit relation for $\log_{10}(\lambda_{\rm Edd,2})$ versus $r_{\rm p}$ obtained by excluding the outlier point, since it is consistent with the result including the outlier and provides higher statistical significance:

$$\log_{10}(\lambda_{\rm Edd,2}) = (-2.3 \pm 0.6) \cdot \left(\frac{r_{\rm p}}{100\,{\rm kpc}}\right) + (-0.78 \pm 0.33). \quad (4)$$

The bottom left-hand panel of Figure 7 shows the best fit for $\lambda_{\rm Edd,2}$ and its uncertainty region at $\pm 3\sigma$ as a dashed red line and a shaded yellow band, respectively, if we consider the outlier. We also show the best fit and uncertainty region for $\lambda_{\rm Edd,2}$ as a dotted black line and shaded grey band in the bottom left-hand panel of Figure 7, if we exclude the outlier. This result suggests that accretion processes for the less massive SMBH may become stronger as it approaches its more massive companion. Such accretion processes may be triggered by gas inflow onto the less massive SMBH induced by gravitational and hydrodynamical torques from the more massive companion. This scenario agrees with the higher obscuration found in late-stage mergers from the X-ray spectral analysis (see Section 4.2.1), assuming that part of the gas that is obscuring the nucleus also fuels SMBH accretion. These findings agree with hydrodynamical simulations of galaxy mergers, which show that AGN activity and obscuration increase during the merger stages (Capelo et al. 2015, 2017; Blecha et al. 2018).

5. Summary and conclusions

We investigated the properties of nearby ($z < 0.1$) X-ray-selected dual AGN and AGN-galaxy pairs using XMM-Newton and Chandra ($r_{\rm p} = 1$–100 kpc, $\Delta z < 10^{-3}$). We performed spectral extraction and analysis in the X-ray band for 52 AGN in the AGN-AGN sample and X-ray spectral analysis for 71 AGN in the AGN-galaxy sample, as well as optical spectroscopic analysis for 46 AGN in the AGN-AGN sample. From multi-wavelength spectral analysis, we derive key physical quantities that characterise AGN in pairs, such as the line-of-sight obscuration, bolometric luminosity, and Eddington ratio. We additionally performed a statistical comparison between the dual-AGN sample and a control sample of inactive galaxies in pairs and compared the properties of our dual-AGN sample with those of isolated AGN.

– Amongst all X-ray-selected AGN (see Section 2), ~10% are found to be in pairs (with either a galaxy or an AGN as a companion). The fraction of AGN paired with a galaxy is ~6%, while the fraction of dual AGN is ~4% (see Figure 3). This fraction reduces to ~2% in late-stage mergers ($r_{\rm p} <$ 30 kpc).
– Using thresholds on XMM-Newton hardness ratios in four energy bands (HR3 > 0 and HR4 > 0.2), we find that ≳44% of isolated AGN are absorbed with $N_{\rm H} > 10^{22}$ cm^{-2}. This fraction should be regarded as a lower limit, since our selection criteria do not allow identification of the full population of Compton-thick sources (including those with HR3 < 0 and HR4 < 0.2).
– We find that ~55% of AGN in pairs are absorbed with $N_{\rm H} > 10^{22}$ cm^{-2}, with a mean value of $\sim 1.8 \times 10^{23}$ cm^{-2}. This fraction is ~60% for AGN-AGN pairs and ~50% for AGN-galaxy pairs. The fraction of Compton-thick AGN in pairs is ~6%. Overall, our results suggest that the fraction of obscured AGN in pairs is higher than in isolated AGN, although the comparison remains uncertain because we only have a lower limit for the fraction of absorbed isolated AGN, which could therefore be higher than 44%.
– We find that the fraction of absorbed AGN in pairs ($N_{\rm H} > 10^{22}$ cm^{-2}) increases as galaxy interactions progress. Specifically, the fractions are ~65% (~70% for AGN-AGN pairs and ~61% for AGN-galaxy pairs) in late merger stages, ~56% (~70% for AGN-AGN pairs and ~45% for AGN-galaxy pairs) in the middle merger stages, and ~35% (~30% for AGN-AGN pairs and ~39% for AGN-galaxy pairs) in early merger stages (see Figure 5). Although we did not find a clear correlation between $N_{\rm H}$ and the projected spatial separation, these results indicate that obscuration becomes more common as galaxy pairs evolve towards late merger stages.
– We quantified the excess of AGN pairs relative to inactive galaxy pairs in bins of projected spatial separation. In each bin, the excess is defined as $f^{\rm AGN}_{\rm bin}/f^{\rm gal}_{\rm bin}$, where $f^{\rm AGN}_{\rm bin}$ and $f^{\rm gal}_{\rm bin}$ are the fractions of AGN and galaxy pairs in each bin normalised by the total number of AGN or galaxies in pairs plus isolated systems (i.e. number of AGN/galaxies in the bin over the total number of AGN or galaxies in pairs plus

isolated systems). We estimated the excess for all AGN in pairs, for only obscured AGN in pairs, and for and only unobscured AGN in pairs. We find that AGN pairs are more common than inactive galaxy pairs on average, but we find a significant correlation between AGN excess and r_p only for obscured AGN (see Figure 6). This suggests that mergers may impact AGN triggering, especially for obscured AGN, and reflects the higher obscuration regime for AGN in close pairs.
- We investigated the relation between the bolometric luminosity of AGN in AGN-AGN pairs relative to the projected spatial separation. We find a clear increase in the bolometric luminosity of the less massive BH in each pair as the interaction progresses. Specifically, we find a significant anti-correlation between $L_{bol,2}$ and r_p (with a Pearson coefficient of $r \sim -0.77$ and a p-value $\sim 2 \times 10^{-5}$, see the top left-hand panel of Figure 7 and Table 1). We also used simulations to verify that this anti-correlation is not driven by a possible bias in AGN selection due to their higher obscuration at the closest separations (with obscured fractions from our analysis; see Figure 5), but it could be due to physical mechanisms occurring during the merger. This anti-correlation is not found for the more massive BHs of the pairs (see the top right-hand panel of Figure 7). These results suggest that mergers preferentially enhance accretion onto the less massive BH, leading to more luminous secondary AGN at the closest separations. The flat trend between BH mass and projected spatial separation (see the left-hand panel of Figure 8) suggests that the increase in bolometric luminosity for BH2 is likely due to enhanced accretion processes triggered by nuclei interaction.
- We find that in most AGN pairs, the less massive BH accretes at higher Eddington ratio λ_{Edd} than its companion (see Figure 8). There is clear evidence of an increase in the Eddington ratio of the less massive BH of the pair as the projected spatial separation between the nuclei decreases (see the bottom left-hand panel of Figure 7), consistent with the observed increase in $L_{bol,2}$ and the lack of any trend between $M_{BH,2}$ and r_p. Conversely, the Eddington ratio of the more massive BH does not increase during the merger phases (see the bottom right-hand panel of Figure 7). Taken together, our findings suggest that galaxy interactions in minor mergers may play an important role in triggering and enhancing AGN activity in the less massive BH, leading to stronger accretion and higher luminosity as the nuclei approach each other.

Data availability

The high-level data underlying this article are derived from public archives (SDSS, XMM-Newton, and Chandra) through standard processing and will be shared on reasonable request to the corresponding author.

Acknowledgements. We would like to thank the referee for the time and for the constructive comments, which have helped us to significantly improve the quality of the manuscript. We acknowledge financial contribution from INAF Large Grant "The Quest for dual and binary massive black holes in the gravitational wave era" (Bando Ricerca Fondamentale INAF 2024) and from INAF Large Grant "Dual and binary supermassive black holes in the multi-messenger era: from galaxy mergers to gravitational waves" (Bando Ricerca Fondamentale INAF 2022). We acknowledge financial support from the ASI-INAF agreement n. 2024-36-HH.1-2025 and n. 2025-29-HH.0. PRC acknowledges support from the Swiss National Science Foundation under the Sinergia Grant CRSII5_213497 (GW-Learn) and fruitful discussions with Massimo Dotti. EB acknowledges the support of the INAF GO grant "A JWST/MIRI MIRACLE: Mid-IR Activity of Circumnuclear Line Emission" and of the "Ricerca Fondamentale 2024" INAF program (mini-grant 1.05.24.07.01). We acknowledge support from PRIN-MUR project "PROMETEUS" financed by the European Union – Next Generation EU, Mission 4 Component 1 CUP B53D23004750006 and C53D2300080006. This research has made use of data obtained from the 4XMM XMM-Newton serendipitous source catalogue compiled by the 10 institutes of the XMM-Newton Survey Science Centre selected by ESA. This research has made use of data obtained from the Chandra Data Archive, observations made by the Chandra X-ray Observatory and published previously in cited articles. This publication has made use of data products from the Wide-field Infrared Survey Explorer, which is a joint project of the University of California, Los Angeles, and the Jet Propulsion Laboratory/California Institute of Technology, funded by the National Aeronautics and Space Administration. Funding for SDSS-III has been provided by the Alfred P. Sloan Foundation, the Participating Institutions, the National Science Foundation, and the U.S. Department of Energy Office of Science. The SDSS-III web site is http://www.sdss3.org. SDSS-III is managed by the Astrophysical Research Consortium for the Participating Institutions of the SDSS-III Collaboration including the University of Arizona, the Brazilian Participation Group, Brookhaven National Laboratory, Carnegie Mellon University, University of Florida, the French Participation Group, the German Participation Group, Harvard University, the Instituto de Astrofisica de Canarias, the Michigan State/Notre Dame/JINA Participation Group, Johns Hopkins University, Lawrence Berkeley National Laboratory, Max Planck Institute for Astrophysics, Max Planck Institute for Extraterrestrial Physics, New Mexico State University, New York University, Ohio State University, Pennsylvania State University, University of Portsmouth, Princeton University, the Spanish Participation Group, University of Tokyo, University of Utah, Vanderbilt University, University of Virginia, University of Washington, and Yale University. FR acknowledges support from ELSA. ELSA Euclid Legacy Science Advanced analysis tools" (Grant Agreement no. 101135203) is funded by the European Union. Views and opinions expressed are, however, those of the author(s) only and do not necessarily reflect those of the European Union or Innovate UK. Neither the European Union nor the granting authority can be held responsible for them. UK participation is funded through the UK Horizon guarantee scheme under Innovate UK grant 10093177.

References

Agazie, G., Anumarlapudi, A., Archibald, A. M., et al. 2023, ApJ, 951, L8
Aggarwal, Y. 2024, MNRAS, 530, 1512
Ahumada, R., Allende Prieto, C., Almeida, A., et al. 2020, ApJS, 249, 3
Aird, J., Coil, A. L., Moustakas, J., et al. 2012, ApJ, 746, 90
Ajith, P., Seoane, P. A., Arca Sedda, M., et al. 2025, JCAP, 2025, 108
Akylas, A., & Georgantopoulos, I. 2021, A&A, 655, A60
Amaro-Seoane, P., Andrews, J., Arca Sedda, M., et al. 2023, Liv. Rev. Relat., 26, 2
Andonie, C., Alexander, D. M., Greenwell, C., et al. 2025, MNRAS, 539, 2202
Antonucci, R. 1993, ARA&A, 31, 473
Arnaud, K. A. 1996, ASP Conf. Ser., 101, 17
Balucinska-Church, M., & McCammon, D. 1992, ApJ, 400, 699
Becker, R. H., White, R. L., & Helfand, D. J. 1995, ApJ, 450, 559
Begelman, M. C., Volonteri, M., & Rees, M. J. 2006, MNRAS, 370, 289
Bentz, M. C., Denney, K. D., Grier, C. J., et al. 2013, ApJ, 767, 149
Bernhard, E., Mullaney, J. R., Aird, J., et al. 2018, MNRAS, 476, 436
Bianchi, S., La Franca, F., Matt, G., et al. 2008, MNRAS, 389, L52
Bianchi, S., Bonilla, N. F., Guainazzi, M., Matt, G., & Ponti, G. 2009, A&A, 501, 915
Bianchi, S., Guainazzi, M., Laor, A., Stern, J., & Behar, E. 2019, MNRAS, 485, 416
Blecha, L., Snyder, G. F., Satyapal, S., & Ellison, S. L. 2018, MNRAS, 478, 3056
Boorman, P. G., Gandhi, P., Buchner, J., et al. 2025, ApJ, 978, 118
Burrows, D. N., Hill, J. E., Nousek, J. A., et al. 2005, Space Sci. Rev., 120, 165
Capelo, P. R., & Dotti, M. 2017, MNRAS, 465, 2643
Capelo, P. R., Volonteri, M., Dotti, M., et al. 2015, MNRAS, 447, 2123
Capelo, P. R., Dotti, M., Volonteri, M., et al. 2017, MNRAS, 469, 4437
Capelo, P. R., Feruglio, C., Hickox, R. C., & Tombesi, F. 2023, Handbook of X-ray and Gamma-ray Astrophysics (Singapore: Springer Nature), 126
Cappellari, M. 2017, MNRAS, 466, 798
Cardelli, J. A., Clayton, G. C., & Mathis, J. S. 1989, ApJ, 345, 245
Cash, W. 1979, ApJ, 228, 939
Chen, S.-J., Wang, J.-X., Kang, J.-L., et al. 2025, ApJ, 995, 197
Colpi, M., Danzmann, K., Hewitson, M., et al. 2024, ArXiv e-prints [arXiv:2402.07571]
Comerford, J. M., Gerke, B. F., Stern, D., et al. 2012, ApJ, 753, 42
Corral, A., Della Ceca, R., Caccianiga, A., et al. 2011, A&A, 530, A42
Cox, I. S., Torres-Albà, N., Marchesi, S., et al. 2023, ApJ, 958, 155

De Rosa, A., Bianchi, S., Bogdanović, T., et al. 2015, MNRAS, 453, 214
De Rosa, A., Vignali, C., Husemann, B., et al. 2018, MNRAS, 480, 1639
De Rosa, A., Vignali, C., Bogdanović, T., et al. 2019, New Astron. Rev., 86, 101525
De Rosa, A., Vignali, C., Severgnini, P., et al. 2023, MNRAS, 519, 5149
Di Matteo, T., Springel, V., & Hernquist, L. 2005, Nature, 433, 604
Duras, F., Bongiorno, A., Ricci, F., et al. 2020, A&A, 636, A73
Eddington, A. S. 1916, MNRAS, 77, 16
Ellison, S., Ferreira, L., Bickley, R., et al. 2025, Open J. Astrophys., 8, 12
EPTA Collaboration, InPTA Collaboration, Antoniadis, J., et al. 2023, A&A, 678, A49
Evans, I. N., Primini, F. A., Glotfelty, K. J., et al. 2010, ApJS, 189, 37
Evans, I. N., Primini, F. A., Miller, J. B., et al. 2020, Am. Astron. Soc. Meet. Abstr., 235, 154.05
Flesch, E. W. 2024, Open J. Astrophys., 7, 6
Foord, A., Gültekin, K., Runnoe, J. C., & Koss, M. J. 2021, ApJ, 907, 71
Fruscione, A., McDowell, J. C., Allen, G. E., et al. 2006, SPIE Conf. Ser., 6270, 62701V
Fu, H., Myers, A. D., Djorgovski, S. G., et al. 2015, ApJ, 799, 72
Gao, F., Wang, L., Pearson, W. J., et al. 2020, A&A, 637, A94
Ge, J.-Q., Hu, C., Wang, J.-M., Bai, J.-M., & Zhang, S. 2012, ApJS, 201, 31
Ge, L., Paltani, S., Eckert, D., & Salvato, M. 2022, A&A, 667, A153
George, I. M., & Fabian, A. C. 1991, MNRAS, 249, 352
Gianolli, V. E., Kim, D. E., Bianchi, S., et al. 2023, MNRAS, 523, 4468
Gierliński, M., & Done, C. 2004, MNRAS, 349, L7
González-Martín, O., Masegosa, J., Márquez, I., Guainazzi, M., & Jiménez-Bailón, E. 2009, A&A, 506, 1107
Greene, J. E., & Ho, L. C. 2005, ApJ, 630, 122
Grimm, H. J., Gilfanov, M., & Sunyaev, R. 2002, A&A, 391, 923
Guainazzi, M., De Rosa, A., Bianchi, S., et al. 2021, MNRAS, 504, 393
Haardt, F., & Maraschi, L. 1993, ApJ, 413, 507
Haardt, F., Maraschi, L., & Ghisellini, G. 1994, ApJ, 432, L95
Harrison, F. A., Craig, W. W., Christensen, F. E., et al. 2013, ApJ, 770, 103
He, L., Hou, M., Li, Z., Feng, S., & Liu, X. 2023, ApJ, 949, 49
Heckman, T. M., Kauffmann, G., Brinchmann, J., et al. 2004, ApJ, 613, 109
HI4PI Collaboration (Ben Bekhti, N., et al.) 2016, A&A, 594, A116
Hopkins, P. F., Hernquist, L., Cox, T. J., et al. 2006, ApJS, 163, 1
Hou, M., Li, Z., & Liu, X. 2020, ApJ, 900, 79
Jaffe, W., Meisenheimer, K., Röttgering, H. J. A., et al. 2004, Nature, 429, 47
Kauffmann, G., Heckman, T. M., Tremonti, C., et al. 2003, MNRAS, 346, 1055
Kim, D. C., Yoon, I., Evans, A. S., et al. 2020, ApJ, 904, 23
Kocevski, D. D., Faber, S. M., & Mozena, M. 2012, ApJ, 744, 148
Kocevski, D. D., Brightman, M., Nandra, K., et al. 2015, ApJ, 814, 104
Koss, M., Mushotzky, R., Veilleux, S., et al. 2011, ApJ, 735, L42
Koss, M., Mushotzky, R., Treister, E., et al. 2012, ApJ, 746, L22
Krimm, H. A., Holland, S. T., Corbet, R. H. D., et al. 2013, ApJS, 209, 14
Lacy, M., Baum, S. A., & Chandler, C. J. 2020, PASP, 132, 035001
Lena, D. 2015, Ph.D. Thesis, Rochester Institute of Technology, New York
Liedahl, D. A., Osterheld, A. L., & Goldstein, W. H. 1995, ApJ, 438, L115
Liu, X., Shen, Y., Strauss, M. A., & Hao, L. 2011, ApJ, 737, 101
Lynden-Bell, D. 1969, Nature, 223, 690
Magdziarz, P., & Zdziarski, A. A. 1995, MNRAS, 273, 837
Mannucci, F., Pancino, E., Belfiore, F., et al. 2022, Nat. Astron., 6, 1185
Mateos, S., Carrera, F. J., Alonso-Herrero, A., et al. 2015, MNRAS, 449, 1422
Matt, G., Perola, G. C., & Piro, L. 1991, A&A, 247, 25
Mauch, T., Murphy, T., Buttery, H. J., et al. 2003, MNRAS, 342, 1117
Mayer, L., Kazantzidis, S., Escala, A., & Callegari, S. 2010, Nature, 466, 1082
Mayer, L., Capelo, P. R., Zwick, L., & Di Matteo, T. 2024, ApJ, 961, 76
McConnell, N. J., & Ma, C.-P. 2013, ApJ, 764, 184
McConnell, D., Hale, C. L., Lenc, E., et al. 2020, PASA, 37, e048
Meisenheimer, K., Tristram, K. R. W., Jaffe, W., et al. 2007, A&A, 471, 453
Mewe, R., Gronenschild, E. H. B. M., & van den Oord, G. H. J. 1985, A&AS, 62, 197
Mewe, R., Lemen, J. R., & van den Oord, G. H. J. 1986, A&AS, 65, 511
Miniutti, G., & Fabian, A. C. 2004, MNRAS, 349, 1435
Nandra, K., & Pounds, K. A. 1994, MNRAS, 268, 405
Netzer, H. 2009, MNRAS, 399, 1907
Osterbrock, D. E., & Ferland, G. J. 2006, Astrophysics of Gaseous Nebulae and Active Galactic Nuclei (Sausalito: University Science Books)
Padovani, P. 2016, A&ARv, 24, 13
Pfeifle, R. W., Satyapal, S., Secrest, N. J., et al. 2019, ApJ, 875, 117
Pfeifle, R. W., Weaver, K. A., Secrest, N. J., Rothberg, B., & Patton, D. R. 2024, ArXiv e-prints [arXiv:2411.12799]
Ponti, G., Cappi, M., Costantini, E., et al. 2013, A&A, 549, A72
Raban, D., Jaffe, W., Röttgering, H., Meisenheimer, K., & Tristram, K. R. W. 2009, MNRAS, 394, 1325
Ranalli, P., Comastri, A., & Setti, G. 2002, ArXiv e-prints [arXiv:astro-ph/0202241]
Rees, M. J. 1984, ARA&A, 22, 471
Reines, A. E., & Volonteri, M. 2015, ApJ, 813, 82
Reines, A. E., Greene, J. E., & Geha, M. 2013, ApJ, 775, 116
Ricci, C., Ueda, Y., Koss, M. J., et al. 2015, ApJ, 815, L13
Ricci, C., Bauer, F. E., Treister, E., et al. 2017a, MNRAS, 468, 1273
Ricci, C., Trakhtenbrot, B., Koss, M. J., et al. 2017b, ApJS, 233, 17
Ricci, C., Privon, G. C., Pfeifle, R. W., et al. 2021, MNRAS, 506, 5935
Salpeter, E. E. 1964, ApJ, 140, 796
SAS Development Team 2014, Astrophysics Source Code Library [record ascl:1404.004]
Satyapal, S., Ellison, S. L., McAlpine, W., et al. 2014a, MNRAS, 441, 1297
Satyapal, S., Secrest, N. J., McAlpine, W., et al. 2014b, ApJ, 784, 113
Satyapal, S., Secrest, N. J., Ricci, C., et al. 2017, ApJ, 848, 126
Satyapal, S., Abel, N. P., & Secrest, N. J. 2018, ApJ, 858, 38
Schartel, N., González-Riestra, R., Kretschmar, P., et al. 2022, XMM-Newton (Singapore: Springer Nature), 1
Schulz, E. 2017, ApJ, 836, 151
Scialpi, M., Mannucci, F., Marconcini, C., et al. 2024, A&A, 690, A57
Secrest, N. J., Dudik, R. P., Dorland, B. N., et al. 2015, ApJS, 221, 12
Severgnini, P., Caccianiga, A., & Della Ceca, R. 2012, A&A, 542, A46
Shakura, N. I., & Sunyaev, R. A. 1973, A&A, 24, 337
Shimwell, T. W., Röttgering, H. J. A., Best, P. N., et al. 2017, A&A, 598, A104
Silverman, J. D., Kampczyk, P., Jahnke, K., et al. 2011, ApJ, 743, 2
Smith, K. L., Shields, G. A., Bonning, E. W., et al. 2010, ApJ, 716, 866
Soltan, A. 1982, MNRAS, 200, 115
Stern, D., Assef, R. J., Benford, D. J., et al. 2012, ApJ, 753, 30
Treister, E., Schawinski, K., Urry, C. M., & Simmons, B. D. 2012, ApJ, 758, L39
Truemper, J. 1982, Adv. Space Res., 2, 241
Ueda, Y., Eguchi, S., Terashima, Y., et al. 2007, ApJ, 664, L79
Ursini, F., Marinucci, A., Matt, G., et al. 2023, MNRAS, 519, 50
Vazdekis, A., Koleva, M., Ricciardelli, E., Röck, B., & Falcón-Barroso, J. 2016, MNRAS, 463, 3409
Volonteri, M., Pfister, H., Beckmann, R., et al. 2022, MNRAS, 514, 640
Wachter, K., Leach, R., & Kellogg, E. 1979, ApJ, 230, 274
Wang, J. X., Malhotra, S., Rhoads, J. E., & Norman, C. A. 2004, ApJ, 612, L109
Wang, J.-M., Chen, Y.-M., Hu, C., et al. 2009, ApJ, 705, L76
Wasleske, E. J., & Baldassare, V. F. 2024, ApJ, 971, 68
Watson, M. G., Auguères, J. L., Ballet, J., et al. 2001, A&A, 365, L51
Webb, N. A., Coriat, M., Traulsen, I., et al. 2020, A&A, 641, A136
Weisskopf, M. C. 2012, Proc. SPIE, 8443, 84430Y
Woniak, P. R., Vestrand, W. T., Akerlof, C. W., et al. 2004, AJ, 127, 2436
Wright, E. L., Eisenhardt, P. R. M., Mainzer, A. K., et al. 2010, AJ, 140, 1868
York, D. G., Adelman, J., Anderson, J. E., et al. 2000, AJ, 120, 1579

Appendix A: Spectral analysis: tables of results

Tables A.1 and A.2 report the results of X-ray and optical spectral analysis on single sources as described in Section 3.

Appendix B: Hardness ratio simulations

The X-ray HR, defined as $(H-S)/(H+S)$, being H and S the counts per second in a hard and in a soft energy band, respectively, is strictly connected with $N_{\rm H}$ and its variability (e.g. Severgnini et al. 2012; De Rosa et al. 2023; Cox et al. 2023). Indeed, the higher the column density is, the more the primary emission of the AGN is suppressed, mainly decreasing the counts per second in the softer band, so that HR increases. Because of the different instrument characteristics, the bands in which HR is computed are H = 4.5–10 keV, S = 2–4.5 keV (HR4), and H = 2–4.5 keV, S = 1–2 keV (HR3) for XMM-Newton, and H = 2–8 keV, S = 0.5–2 keV for Chandra. For XMM-Newton, HR4 is more sensitive to high obscuration ($N_{\rm H} > 10^{23}$ cm^{-2}), while HR3 is more sensitive to moderate obscuration (e.g. the Compton-thin regime, $N_{\rm H} = 10^{22}$–10^{24} cm^{-2}). However, in any band, there is no unique correlation between HR and $N_{\rm H}$, since when $N_{\rm H}$ starts to enter the high absorbed regime, HR starts to decrease again (see Figure B.1).

We performed simulations with Xspec with the aim of deriving the correlation between XMM-Newton HR3 and HR4 with $N_{\rm H}$ (that we used to estimate the fraction of absorbed AGN in the PS). We set the number of simulations to 50,000, in order to have a high number of data-points. For each simulation, we generated a fake spectrum from which we extracted the counts per second in the bands of interest using the BLM described in Section 3. Each simulated spectrum is created using different values for $N_{\rm H}$, Γ^H, Γ^S, K^H, and K^S. $N_{\rm H}$ was varied in order to have data-points from $N_{\rm H} = 10^{20}$ cm^{-2} to $N_{\rm H} = 10^{24}$ cm^{-2}. We decided to exclude $N_{\rm H} > 10^{24}$ cm^{-2}, since in the CT regime the primary component of the AGN is totally suppressed in the observed X-ray bands (and, given the low redshift selection of the candidates, it would be not visible in XMM-Newton energy range). We varied the Γ^H value in the range 1.5–2.2, based on previous studies of AGN photon index distributions (Bianchi et al. 2009; Corral et al. 2011; Ge et al. 2022). In the hard and soft power law, K^H and K^S were varied in order to have $0.001 < K^S/K^H < 0.01$. We fixed the Milky Way hydrogen column density to $N_{\rm H}^{\rm Gal} = 10^{20}$ cm^{-2}. Finally, the redshift was fixed to the mean value for the PS ($z \sim 0.05$). This choice is justified with the fact that although HR evolves with redshift (Wang et al. 2004), it does not depend on redshift in the range we are studying. The results of our simulations are shown in Figure B.1, where the degeneracy in the HR-$N_{\rm H}$ relation is clear, especially for HR3. Moreover, different values of Γ^H and K^S/K^H up to $N_{\rm H} = 10^{24}$ cm^{-2} produce different curves, as one can notice looking at the colour-code. Despite the previously described limitations when using HR as a proxy for $N_{\rm H}$, through our simulations we found that, depending on the Γ^H value, a source enters the Compton-thin regime for HR3 ∼ −0.2 – 0.1 (left-hand panel of Figure B.1) and the highly obscured regime ($N_{\rm H} > 10^{23}$ cm^{-2}) for HR4 ∼ 0–0.25 (right-hand panel of Figure B.1). Choosing a typical Γ^H = 1.9, we can put a threshold on HR3 ≥ 0 and HR4 ≥ 0.2 to distinguish between un-obscured and obscured/highly obscured sources, respectively, and use this values of HR to estimate the fraction of Compton-thin isolated AGN in the PS.

Appendix C: Simulations for XMM-Newton and Chandra source detectability

AGN in pairs at close separations (i.e. $r_{\rm p} < 30$ kpc) were found to suffer from higher obscuration with respect to that in early merger stage (see Sections 4.1, 4.2.1). This could mean that low-luminosity AGN may be not detected by XMM-Newton and Chandra, especially at the closest separations, if their X-ray fluxes fall below the detection limit of the available observations (see Section 2.1) due to a possible high obscuration. This could consequentially lead to a number of missing low-luminosity AGN at close separations, resulting in a potential bias for the correlation between $\log_{10}(L_{\rm bol,2})$ and $r_{\rm p}$. In fact, if such kind of bias were confirmed, this would imply that the observed linear increase of $\log_{10}(L_{\rm bol,2})$ with decreasing $r_{\rm p}$ would be possibly driven by selection effects. To quantify how a selection bias would affect our dual-AGN sample, we performed simulations in Xspec to reproduce an unbiased population of AGN. To this goal, we simulated AGN spectra without imposing any constraint on the X-ray fluxes, but only requiring that each fake spectrum should satisfy the X-ray definition to be associated with an AGN source (i.e. intrinsic luminosity $L(2-10\,{\rm keV}) \geq 10^{40}$ erg s^{-1}). This ensured us to not exclude possible sources with X-ray fluxes below 10^{-15} erg s^{-1} cm^{-2} (for XMM-Newton) and 10^{-16} erg s^{-1} cm^{-2} (for Chandra), which are the possible missing AGN from our selection (see Section 2.1). For the simulations, we assumed as fitting model a simple absorbed power-law, $f(E) = e^{-N_{\rm H}\sigma}KE^{-\Gamma^H}$ (*ztbabs* × *powerlaw* in Xspec), varying the values of the photon index Γ in the range 1.5 – 2.2, according to previous studies on AGN photon index distributions (Bianchi et al. 2009; Corral et al. 2011; Ge et al. 2022). The normalisation K was instead varied in order to have 10^{40} erg s^{-1} ≤ $L(2-10\,{\rm keV})$ ≤ 10^{43} erg s^{-1} (to match the intrinsic luminosities of our sample), depending on the simulated $N_{\rm H}$ value (described below). We used this X-ray luminosity to estimate the bolometric luminosity of each AGN using Duras et al. (2020). The redshift values for the *ztbabs* component were varied in the range of our selection ($0.01 \lesssim z < 0.1$). We then included the effect of obscuration based on our results described in Section 4.1: we simulated three sets of data points in which we required the fraction of absorbed AGN to be 70%, 70%, and 30%, corresponding to the late, middle, and early stage of merger, respectively (see Figure 5). The value of $r_{\rm p}$ for each simulated AGN was randomly assigned in each bin of separation 0 – 30 kpc, 30 – 60 kpc and 60 – 100 kpc, depending on the belonging set. The $N_{\rm H}$ corresponding to absorbed AGN was varied in the range 10^{22} cm^{-2} ≤ $N_{\rm H}$ ≤ 10^{24} cm^{-2}. The number of simulations was set to 500 for each bin of obscuration/separation both for XMM-Newton and Chandra, so that we had a total number of 3000 simulated data-points over all the separations, and an equal number of data-points in each bin. These simulations thus produced a complete population of AGN at all separations, that is unbiased against the absorption. Finally, we imposed flux cuts matching our selection criteria (see Section 2.1), in order to reproduce our observed AGN sample and include the possible obscuration bias. If a bias due to absorption exists, we thus expect that after the flux cut the number of low-luminosity AGN would be significantly reduced for the separations more affected by obscuration (i.e. the ones in the late state of merger), mimicking the observed trend between $L_{\rm bol,2}$ and $r_{\rm p}$ shown in the left-hand panel of Figure 7. As a result, in Figure C.1 is shown the average simulated bolometric luminosity in each bin of projected spatial separation, after the flux cut on the sources. A slight increase of the average bolometric luminosity with decreasing

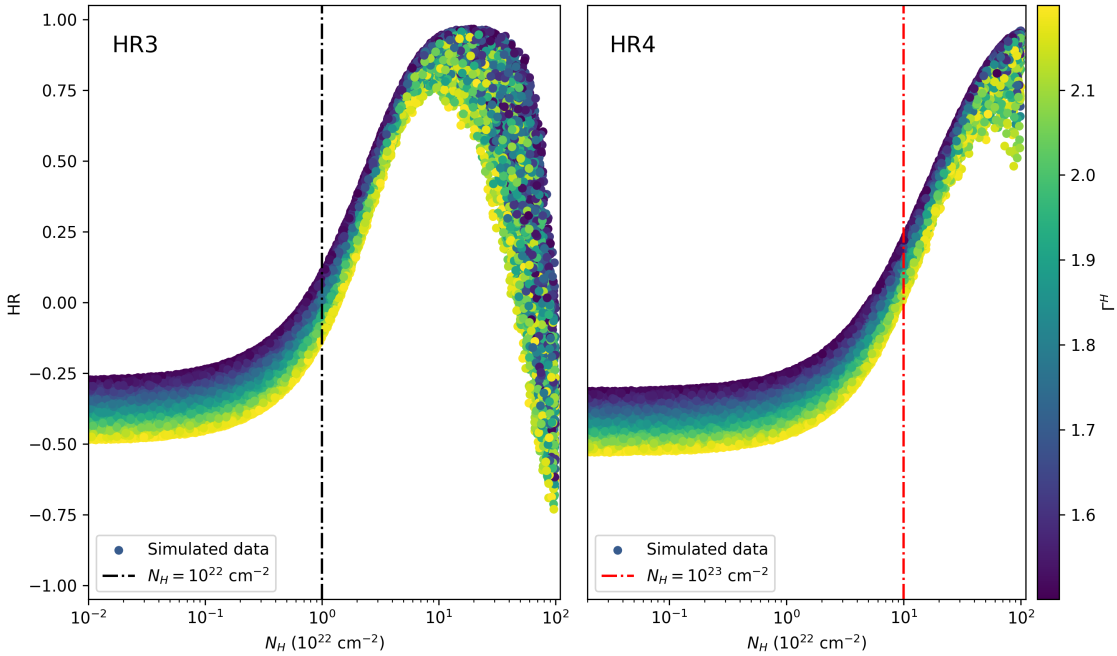

Fig. B.1. Results from the HR3$-N_{\rm H}$ (left-hand panel) and HR4$-N_{\rm H}$ (right-hand panel) simulations. Data-points are colour-coded based on the Γ^H value (colour bar on the right). The black and red, vertical, dashed lines represent the values $N_{\rm H} = 10^{22}$ cm^{-2} and 10^{23} cm^{-2}, respectively.

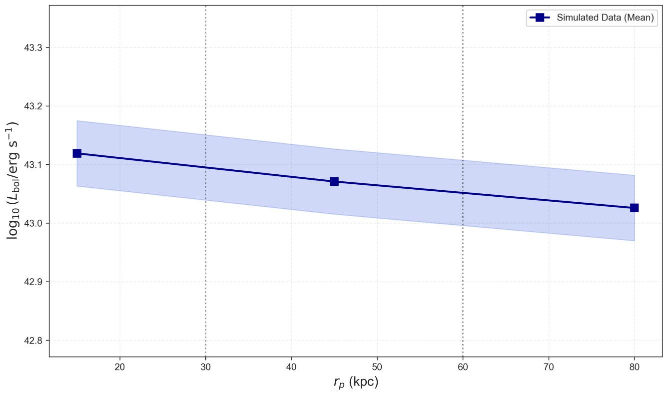

Fig. C.1. Average simulated bolometric luminosity in each bin of projected spatial separation after the cuts on AGN fluxes. The shaded-blue region represents the errors on the mean bolometric luminosity in each bin.

$r_{\rm p}$ is visible (as expected after removing low-luminosity sources that are more distributed in the first and second bin), but this is only marginal (of the order of ~ 0.1 dex between the early and late state of merger) and not statistically significant. As a further test, we also artificially increased the fraction of obscured AGN up to 95% in the bin $0 - 30$ kpc when performing the simulations, in order to consider a worst-case scenario of obscuration bias. Again, we did not find appreciable changing on the average bolometric luminosities between the early and late stage of merger, after the flux cuts. This means that the obscuration bias alone is not able to reproduce our observed trend between bolometric luminosity and separation of BH2 (see the upper, left-hand panel of Figure 8). This is in agreement with the fact that a merger-driven physical mechanism is affecting the increase of bolometric luminosity for close pairs.

Table A.1. Results of the X-ray spectral analysis described in Section 3.

[a]IAUNAME	[b]z	[c]r_p (kpc)	[d]Γ^H	[e]Γ^S	[f]N_H (10^{22} cm^{-2})	[g]F_X^{Obs} (10^{-14} erg s^{-1} cm^{-2})	[h]L^{Unabs}(2–10 keV) (10^{41} erg s^{-1})	[i]Net counts (cts)	[l]Opt. spec.
2CXO J135602.8+182218	0.051	3.9	1.8 ± 0.2	*	54^{+16}_{-13}	32 ± 4	103^{+17}_{-14}	1267 ± 36	✗
2CXO J135602.6+182217	0.051	3.9	1.9^f	$2.5^{+0.5}_{-0.4}$	34^{+8}_{-6}	22^{+3}_{-10}	48 ± 6	324 ± 18	✗
2CXO J121346.0+024841‡	0.073	4.8	2.1 ± 0.6	-	-	0.9 ± 0.2	1.3 ± 3	15 ± 5	✓
2CXO J121345.9+024838‡	0.073	4.8	1.9^f	-	< 0.6	0.7 ± 0.2	1.1 ± 4	11 ± 4	✗
2CXO J133817.8+481640‡	0.028	6.4	1.9^f	-	6.8 ± 3.8	24.6 ± 2	4.0	205 ± 15	✓
2CXO J133817.3+481632‡	0.028	6.4	1.6 ± 0.3	-	> 200	2.2 ± 0.9	130^{+270}_{-80}	95 ± 11	✓
2CXO J121417.8+293143	0.064	7.9	1.9^f	$2.0^{+1.2}_{-1.3}$	25^{+13}_{-7}	140 ± 20	370 ± 60	215 ± 15	✓
2CXO J090714.6+520350‡	0.060	8.9	1.5 ± 0.7	-	$2.5^{+1.4}_{1.1}$	13 ± 1	16.0 ± 0.1	121 ± 12	✓
2CXO J090714.4+520343‡	0.060	8.9	1.9^f	-	18^{+16}_{-12}	6.4 ± 1.1	16 ± 3	42 ± 7	✓
2CXO J133440.7-232645	0.033	10.5	$1.1^{+1.2}_{-0.4}$	-	< 1.5	40 ± 7	$9.8^{+2.2}_{-1.8}$	91 ± 10	✗
2CXO J133439.6-232647	0.034	10.5	1.9^f	*	15^{+3}_{-2}	300 ± 30	170^{+20}_{-10}	366 ± 20	✗
2CXO J032512.9+404152	0.048	12.0	2.0^f	-	0.5 ± 0.3	16^{+3}_{-2}	$9.5^{+0.6}_{-1.3}$	152 ± 12	✗
2CXO J032512.2+404202	0.048	12.0	1.1 ± 0.4	*	$6.7^{+1.4}_{-1.0}$	390^{+20}_{-30}	280^{+10}_{-20}	957 ± 31	✗
2CXO J110018.0+100257	0.036	12.6	$2.4^{+0.6}_{-0.5}$	-	< 0.1	3.0 ± 0.5	0.9 ± 0.2	92 ± 10	✓
2CXO J145051.5+050652	0.028	12.6	1.9^f	3.3 ± 0.3	182^{+167}_{-92}	24 ± 10	240 ± 100	224 ± 15	✓
2CXO J012357.0-350409	0.019	13.9	1.4 ± 0.5	-	< 0.1	6.2 ± 1.4	0.5 ± 0.1	62 ± 8	✗
2CXO J012354.3-350355	0.019	13.9	1.5^f	-	0.9 ± 0.1	760^{+40}_{-20}	67 ± 2	4964 ± 70	✗
2CXO J020920.8-100759	0.013	15.0	1.9^f	*	43^{+24}_{-13}	32 ± 7	5.7 ± 1.3	81 ± 9	✓
2CXO J020924.5-100809	0.013	15.0	2.2^f	$3.1^{+1.6}_{-1.2}$	49^{+27}_{-17}	31 ± 7	7.3 ± 1.5	141 ± 12	✗
2CXO J181611.6+423937	0.041	23.2	1.9^f	*	$3.6^{+0.4}_{-0.2}$	240 ± 10	130 ± 10	4308 ± 66	✗
2CXO J181609.3+423922	0.042	23.2	1.9^f	-	46^{+14}_{-10}	33 ± 6	61 ± 10	137 ± 12	✗
2CXO J132809.9-271954	0.042	28.0	$1.8^{+0.3}_{-0.2}$	-	0.8 ± 0.2	280 ± 20	120 ± 10	770 ± 28	✗
2CXO J132807.7-272006	0.042	28.0	1.3^f	*	3.9^{+3}_{-2}	200 ± 30	100 ± 10	412 ± 20	✗
4XMM J094548.3-142204	0.008	29.0	1.6 ± 0.1	-	< 0.03	28 ± 1	0.4 ± 0.2	2519 ± 51	✗
2CXO J094541.9-141934	0.008	29.0	1.1 ± 0.1	-	0.2 ± 0.1	310 ± 10	4.4 ± 0.2	4747 ± 70	✗
4XMM J094554.4+423818‡	0.075	30.3	1.9^f	-	24^{+8}_{-6}	19 ± 2	69 ± 3	1275 ± 37	✓
4XMM J094554.4+423840‡	0.075	30.3	2.4 ± 0.1	-	< 0.02	50 ± 3	70 ± 3	21450 ± 150	✓
4XMM J120445.3+311130‡	0.025	31.0	1.9^f	-	24^{+150}_{-12}	3.0 ± 1.1	$1.1^{+0.7}_{-0.6}$	154 ± 20	✓
4XMM J120443.3+311037‡	0.025	31.0	1.7 ± 0.4	-	3.7 ± 0.5	263 ± 6	31 ± 1	16517 ± 137	✓
4XMM J121958.9-355735	0.057	35.6	$3.3^{1.4}_{-1.2}$	*	> 30	3.0 ± 1.5	16 ± 8	211 ± 17	✗
4XMM J121957.3-355801	0.058	35.6	$1.8^{+0.6}_{-0.5}$	-	< 0.01	1.8 ± 0.4	1.4 ± 0.4	181 ± 16	✗
2CXO J091338.8-101919	0.055	38.8	$3.1^{+0.8}_{-0.7}$	-	< 0.01	0.8 ± 0.2	0.6 ± 0.1	82 ± 9	✗
4XMM J103855.9+392157‡	0.055	42.9	1.9^f	-	> 100	1.6 ± 1.0	70	182 ± 14	✓
4XMM J103853.3+392151‡	0.055	42.9	1.6 ± 0.1	-	< 0.03	55 ± 5	42 ± 2	6534 ± 80	✓
4XMM J100135.8+033648‡	0.043	45.3	1.9^f	-	16^{+31}_{-10}	6.3 ± 1.1	4.6 ± 2	260 ± 29	✓
4XMM J162644.4+142253‡	0.048	51.3	1.9^f	-	6^{+12}_{-4}	1.6 ± 0.8	1.2 ± 0.8	162 ± 15	✓
4XMM J162640.9+142243‡	0.048	51.3	1.9^f	-	67^{+150}_{-50}	2.3 ± 1	8^{+3}_{-7}	364 ± 20	✓
4XMM J145627.4+211956‡	0.044	59.2	1.9 ± 0.9	-	75^{+28}_{-23}	8.6 ± 2.0	37^{+2}_{-13}	602 ± 25	✓
4XMM J145631.3+212030‡	0.044	59.2	1.9^f	-	> 100	2.3 ± 0.5	70	459 ± 32	✓
4XMM J093402.8+100631	0.010	60.1	1.9^f	$4.2^{+2.6}_{-1.5}$	18^{+5}_{-4}	25 ± 4	1.4 ± 0.2	455 ± 25	✓
4XMM J093346.0+100909	0.011	60.1	$1.8^{+0.6}_{-0.3}$	-	< 0.2	5.4 ± 0.7	0.12 ± 0.02	838 ± 32	✓
2CXO J201010.8-481713	0.010	76.6	$1.9^{+0.2}_{-0.1}$	-	< 0.01	15 ± 2	0.33 ± 0.03	496 ± 22	✗
2CXO J200954.0-482246	0.010	76.6	1.6^f	-	< 0.08	11 ± 1	0.24 ± 0.02	1556 ± 39	✗
4XMM J165105.6-012748	0.041	82.3	1.8^f	*	72^{+32}_{-23}	31 ± 5	93^{+17}_{-15}	765 ± 34	✗
4XMM J165105.8-012926	0.041	82.3	$1.7^{+1.1}_{-0.3}$	$1.4^{+1.9}_{-1.2}$	$4.8^{+3.0}_{-1.3}$	78 ± 5	41 ± 3	1768 ± 47	✗
4XMM J232903.9+033159	0.017	87.8	2.3^f	*	45^{+19}_{-14}	28 ± 5	11 ± 2	1493 ± 47	✗
4XMM J232846.6+033041	0.016	87.8	2.0^f	-	< 0.01	54 ± 2	3.1 ± 0.1	6343 ± 90	✗
4XMM J100236.6+324224‡	0.051	88.1	$2.2^{+0.9}_{-0.6}$	-	< 0.4	10 ± 1	4.7 ± 1	2359 ± 93	✓
4XMM J082321.6+042221‡	0.031	88.7	$3.0^{+0.5}_{-0.4}$	-	$0.6^{+1.4}_{-0.3}$	10 ± 1	$2.2^{+0.4}_{-0.8}$	8871 ± 125	✓
4XMM J102141.8+130551	0.076	94.4	1.9^f	-	< 0.05	0.4 ± 0.2	0.6 ± 0.3	45 ± 11	✓
4XMM J102142.6+130654	0.077	94.4	$1.7^{+0.6}_{-0.5}$	-	< 0.1	1.4 ± 0.4	2.0 ± 0.5	179 ± 17	✓
2CXO J085125.8+393541	0.041	94.6	1.6 ± 0.5	-	< 0.01	4.6 ± 1	1.8 ± 0.4	61 ± 8	✓

(a) Name of the source; (b) redshift; (c) projected spatial separation between the nuclei; (d) photon index of the primary component; (e) photon index of the soft power law; (f) hydrogen column density; (g) observed flux in the 2–10 keV band; (h) de-absorbed luminosity in the 2–10 keV band; (i) net counts of the spectrum in the 0.2–12 keV and 0.5–8 keV bands for XMM-Newton and Chandra, respectively; (l) check for availability of SDSS optical spectrum. Sources marked with ✓/✗ have/do not have an optical spectrum available from SDSS. ‡ sources are the AGN in the De Rosa et al. (2023) sample. The superscripts f for the values of Γ^H and Γ^S mean that the value was fixed either at a typical value of 1.9 or at the best-fit value. When the soft photon index was fixed to the hard photon index value, it is marked with *. If the soft component was not included in the model, or it refers to a source from De Rosa et al. (2023), we marked it with -.

Table A.2. Results of the optical spectral analysis described in Section 3.

(a)IAUNAME	(b)$F(\mathrm{H}\alpha)$ (10^{-16} erg s^{-1} cm^{-2})	(c)$F(\mathrm{H}\beta)$ (10^{-16} erg s^{-1} cm^{-2})	(d)$F([\mathrm{O}\,III])$ (10^{-16} erg s^{-1} cm^{-2})	(e) $\log_{10}(M_{\mathrm{BH}}/\mathrm{M}_\odot)$	(f)L_{bol} (10^{42} erg s^{-1})	(g)X-ray spec.
J133817.8+481640	$(1.0 \pm 0.4) \times 10^3$	386 ± 4	619 ± 6	8.9 ± 0.8	6.8 ± 2.4	✓
J133817.3+481632	467 ± 5	83 ± 5	537 ± 7	8.2 ± 0.5	350 ± 220	✓
J121418.2+293146	60 ± 1	22 ± 1	208 ± 1	8.0 ± 0.4	59 ± 2	✗
J121417.8+293143	511 ± 5	182 ± 5	$2 \times 10^3 \pm 7$	7.5 ± 1.7	$(1.9 \pm 0.3) \times 10^3$	✓
J090714.4+520343	37 ± 1	10 ± 1	66 ± 1	7.9 ± 0.4	32 ± 6	✓
J090714.6+520350	59 ± 1	15 ± 1	49 ± 1	7.0 ± 0.5	55 ± 2	✓
J110018.0+100257	123 ± 1	15 ± 1	47 ± 1	8.1 ± 0.4	1.0 ± 0.2	✓
J110019.1+100250	39 ± 1	5.6 ± 0.3	40 ± 1	8.0 ± 0.4	94 ± 15	✗
J145050.6+050710	17 ± 1	2.5 ± 0.3	4.2 ± 0.4	8.0 ± 0.4	24 ± 11	✗
J145051.5+050652	442 ± 2	124 ± 2	821 ± 2	7.8 ± 0.4	$(1.1 \pm 0.4) \times 10^3$	✓
J120157.8+295945	6.0 ± 0.4	1.8 ± 0.4	5.9 ± 0.5	8.5 ± 0.4	9.5 ± 7.3	✗
J120157.8+295927	11 ± 1	2.9 ± 0.3	6.2 ± 0.4	6.7 ± 0.5	25 ± 9	✗
J094554.4+423840	348 ± 2	134 ± 2	74 ± 2	8.8 ± 0.4	212 ± 9	✓
J094554.4+423818	141 ± 1	38 ± 1	213 ± 1	7.3 ± 0.4	208 ± 9	✓
J120445.3+311130	17 ± 1	5.5 ± 0.6	17 ± 1	7.1 ± 0.4	1.2 ± 0.6	✓
J120443.3+311037	412 ± 3	124 ± 3	$(1.4 \pm 0.4) \times 10^3$	7.1 ± 0.4	74 ± 1	✓
J011834.4-000939	18 ± 1	4.3 ± 0.5	5.4 ± 0.6	8.1 ± 0.4	63 ± 27	✗
J011832.8-000936	2.8 ± 0.3	8.6 ± 0.4	68 ± 1	7.0 ± 0.4	35 ± 1	✗
J103853.3+392151	48 ± 1	18 ± 1	55 ± 1	8.2 ± 0.5	109 ± 5	✓
J103855.9+392157	30 ± 1	9.1 ± 0.3	138 ± 1	6.4 ± 0.4	212 ± 1	✓
J100133.4+033731	2.6 ± 0.4	1.1 ± 0.4	4.6 ± 0.5	7.7 ± 0.4	1.4 ± 0.5	✗
J100135.8+033648	71 ± 1	20 ± 1	80 ± 1	7.1 ± 0.4	6.7 ± 3.6	✓
J162644.4+142253	4.6 ± 0.5	1.1 ± 0.5	4.2 ± 0.4	7.3 ± 0.4	1.3 ± 0.1	✓
J162640.9+142243	43 ± 1	12 ± 1	181 ± 1	7.0 ± 0.4	13 ± 12	✓
J145631.3+212030	47 ± 1	9.9 ± 0.8	181 ± 1	7.1 ± 0.4	212 ± 1	✓
J145627.4+211956	13 ± 1	4.5 ± 0.4	41 ± 1	6.6 ± 0.4	93 ± 33	✓
J015235.9-083139	9.5 ± 0.6	2.7 ± 0.6	6.5 ± 0.7	8.2 ± 0.4	9.6 ± 7.9	✗
J015235.2-083233	29 ± 1	10 ± 1	39 ± 1	6.7 ± 0.4	18 ± 1	✗
J093346.0+100909	155 ± 2	44 ± 2	73 ± 2	8.4 ± 0.4	0.9 ± 0.1	✓
J093402.8+100631	17 ± 1	6.8 ± 1.1	25 ± 1	7.7 ± 0.4	1.6 ± 0.2	✓
J161211.2+293428	6.7 ± 0.3	1.9 ± 0.3	6.7 ± 0.4	8.6 ± 0.4	8.2 ± 4.4	✗
J161216.7+293423	28 ± 1	8.1 ± 0.6	63 ± 1	7.5 ± 0.4	32 ± 9	✗
J160501.3+174632	4.1 ± 0.7	0.9 ± 0.7	4.5 ± 0.8	8.6 ± 0.4	< 2.8	✗
J160508.1+174528	9.3 ± 0.5	2.6 ± 0.5	5.8 ± 0.6	8.0 ± 0.4	4.2 ± 2.9	✗
J134130.5-002512	33 ± 1	7.3 ± 0.4	5.0 ± 0.5	7.9 ± 0.4	109 ± 21	✗
J134133.4-002431	40 ± 2	13 ± 1	123 ± 2	7.5 ± 0.4	58 ± 8	✗
J100236.6+324224	11 ± 2	6.8 ± 1.5	3.1 ± 1.3	9.5 ± 0.4	6.8 ± 1.5	✓
J100230.8+324248	12 ± 1	3.9 ± 0.7	3.2 ± 0.9	9.0 ± 0.4	9.1 ± 5.7	✗
J082321.6+042221	9.2 ± 0.8	5.0 ± 0.8	4.1 ± 1	8.7 ± 0.4	2.7 ± 1	✓
J082329.9+042332	11 ± 1	2.7 ± 0.4	22 ± 1	7.2 ± 0.4	4.9 ± 2.9	✗
J102142.6+130654	52 ± 2	9.5 ± 0.2	4.4 ± 0.3	6.7 ± 0.4	2.4 ± 0.6	✓
J102141.8+130551	23 ± 1	4.8 ± 0.2	17 ± 1	6.6 ± 0.5	0.6 ± 0.3	✓
J085135.7+393523	24 ± 1	5.9 ± 0.5	18 ± 1	7.4 ± 0.4	22 ± 7	✗
J085125.8+393541	38 ± 1	15 ± 1	50 ± 3	4.6 ± 0.7	2.1 ± 0.5	✓
J163102.7+394733	6.0 ± 0.9	2.2 ± 0.9	3.6 ± 0.9	8.3 ± 0.4	1.2 ± 0.5	✗
J163103.4+395015	12 ± 1	2.7 ± 0.6	19 ± 1	7.8 ± 0.4	8.0 ± 6.7	✗

(a) Name of the source; (b), (c), and (d) narrow Hα, Hβ, and [O*III*]5007Å fluxes, respectively; (e) mass of the SMBH, estimated through the $M-\sigma^*$ relation; (f) bolometric luminosity of the AGN, estimated through Duras et al. (2020) when the source had also an X-ray spectral analysis, and through Netzer (2009) otherwise; (g) check on the X-ray spectral analysis. Sources marked with ✓/✗ have/do not have an X-ray spectral analysis.